ELSEVIER

Contents lists available at ScienceDirect

Acta Biomaterialia

journal homepage: www.elsevier.com/locate/actbio



Full length article

In vitro and in vivo evaluation of structurally-controlled silk fibroin coatings for orthopedic infection and in-situ osteogenesis



Zhou Wenhao ^{a,b}, Teng Zhang ^d, Jianglong Yan ^b, QiYao Li ^e, Panpan Xiong ^b, Yangyang Li ^b, Yan Cheng ^{b,*}, Yufeng Zheng ^{b,c,*}

- ^a Northwest Institute for Nonferrous Metal Research, Xi'an 710016, China
- ^b Academy for Advanced Interdisciplinary Studies, Peking University, Beijing 100871, China
- ^c Department of Materials Science and Engineering, College of Engineering, Peking University, Beijing 100871, China
- ^d Department of Orthopedics, Peking University Third Hospital, Beijing 100191, China
- ^e Department of Biomedical Engineering, Materials Research Institute, Huck Institutes of The Life Sciences, The Pennsylvania State University, University Park, PA 16802, United States

ARTICLE INFO

Article history: Received 7 May 2020 Revised 20 August 2020 Accepted 26 August 2020 Available online 2 September 2020

Keywords: Silk fibroin AgNPs, β -sheets structure Antibacterial Osteogenesis

ABSTRACT

Biomedical device-associated infections (BAI) and osteosynthesis are two main complications following the orthopedic implant surgery, especially while infecting bacteria form a mature biofilm, which can protect the organisms from the host immune system and antibiotic therapy. Comparing with the single antibiotics therapeutic method, the combination of silver nanoparticles (AgNPs) and conventional antibiotics exert a high level of antibacterial activity. Nevertheless, one major issue that extremely restricts the potential application of AgNP/antiviotics is the uncontrolled release. Moreover, the lack of osteogenic ability may cause the osteosynthesis. Thus, herein we fabricated a structure-controlled drug-loaded silk fibroin (SF) coating that can achieve the size and release control of AgNPs and high efficient osteogenesis. Three comparative SF-based coatings were fabricated: α -structured coating (α -helices 32.7%,), mstructured coating (β -sheets 28.3%) and β -structured coating (β -sheets 41%). Owning to the high content of α -helices structure and small AgNPs (20 nm), α -structured coating displayed better protein adsorption and hydrophilicity, as well as pH-dependent and long-lasting antibacterial performance. In vitro studies demonstrated that α coating showed biocompatibility (cellular attachment, spreading and proliferation), high ALP expression, collagen secretion and calcium mineralization. Moreover, after one month subcutaneous implantation in vivo, α -structured coating elicited minimal, comparable inflammatory response. Additionally, in a rabbit femoral defect model, α -structured coating displayed a significant improvement on the generation of new-born bone and bonding between the new bone and the tissue, implying a rapid and durable osteointegration. Expectedly, this optimized structure-controlled SF-based coating can be an alternative and prospective solution for the current challenges in orthopedics.

Statement of Significance

In this study, an AgNPs/Gentamycin-loaded structured-controlled silk fibroin coatings were constructed on Ti implant's surface to guarantee the success of implantation even in the face of bacterial infection. In comparison, the α -structured coating had the lowest content of β -sheets structure (19.0%) and the smallest particle size of AgNPs (\sim 20 nm), and owned pH-responsive characteristic due to reversible α -helices structural. Thanks to pH-responsive release of Ag⁺, the α -structure coating could effectively inhibit adhesive bacteria and kill planktonic bacteria by releasing a large amount of reactive oxygen radicals. Through *in vitro* biological results (cell proliferation, differentiation and osteogenic gene expression) and *in vivo*

^{*} Corresponding authors at: Academy for Advanced Interdisciplinary Studies, Peking University, Beijing 100871, China E-mail addresses: chengyan@pku.edu.cn (Y. Cheng), yfzheng@pku.edu.cn (Y. Zheng).

rabbit femur implantation results, the α -structure coating had good biocompatible and osteogenic properties

© 2020 Acta Materialia Inc. Published by Elsevier Ltd. All rights reserved.

1. Introduction

For most orthopedic surgeries, biomedical device-associated infections (BAI) remain a massive and potential issue as it easily trigger further delayed healing, implant failure and repeated surgeries [1]. However, the frequent emergence of multi-resistance bacteria make it even worse, result in relentless spread of restriction to traditional antibiotics [2,3]. Recently, a popular option to overcome bacterial resistance is the combination of traditional antibiotics with AgNPs, a broad spectrum fungicide with potential applications in orthopedic area [4-6]. Different from antibiotics, the antibacterial mechanisms of AgNPs are not specific at a single level but to influence many bacterial structures and metabolic processes at the same time, including inactivate bacterial enzymes, disrupt bacterial metabolic processes and the bacterial cell wall, increase membrane permeability, interact with DNA, and generate reactive oxygen species [7,8]. Therefore, AgNPs could be considered as a suitable candidate for combinations with antibiotics, posing no risk of bacterial resistance. As an aminoglycoside antibiotic, Gentamycin (Gen) can efficiently inhibit infections and biofilm development, and has been proved to work with AgNPs at a relatively low concentration, disclosing the strong synergetic antibacterial effects [9].

Regenerated silk fibroin (SF), a kind of natural proteins harvested from domestic Bombxy mori silkworm silks, has attracted a lot of recent interest in drug-loaded coatings for surface modification of orthopedic implants due to its impressive biological performances, such as tunable degradation rate, easy load of multifarious drugs and long term drug stabilizing [10,11]. In fact, a wide variety of bactericides (e.g. antibiotics, metal nanoparticles and antimicrobial peptides) can be easily embedded in SF coatings by electrostatic force, hydrogen bond or covalent grafting [12-14]. Benefiting from the reductive Tyr-residues of SF chains, SF could in-situ reduce Ag+ to AgNPs under eco-friendly condition with high efficiency [5,15]. Moreover, profiting from unique structure and flexible assembled properties, lots of surface-modified methods, such as electro-spray [16], laser evaporation [17], and layer-by-layer deposition, [18] have been applied to build adaptable SF-based coatings for enhancing the osteogenic differentiation of stem cells and bone formation in bone defect models [19]. As verified, the potentially osteogenic property of SF-based coating derived from its structure striking resemblance to the collagen, an important organic components of natural bone. Also, the amorphous links in the β -sheet structures of SF acted as nucleation sites for the deposition of HA-nanocrystals [20,21]. Also, it has been reported to intervene several gene pathways, which are responsible for regulating the general bone development and remolding [22,23].

When it comes to the intrinsic structure of SF, although several different silk secondary structures are possible, from β -sheets over α -helices to coiled-coil to collagen/polyglycine families, usually SF-based coatings have either a high content of β -sheets or α -helices, depending on their equilibrium state. In detail, highly ordered β -sheet crystalline regions (Silk II) in SF-based coatings are known to modulate degradation kinetics, matrix stiffness, and biocompatible properties [24,25]. From the perspective of osteogenic applications, the secondary structure influence the cell–matrix interaction, the following cellular processes and further osteogenic differentiations. Min et al. proved that SF matrix with higher β -sheet contents showed increased cell adhesion and spreading [26]. Also, mesenchymal progenitor cells embedded in 3D printed con-

structs obtaining higher β -sheet contents of sonicated silk fibroin (25.4%) demonstrated higher propensity toward osteogenic differentiation, compared to tyrosinase-induced cross-linked constructs (having only 14% β -sheet content) [27]. Reversely, the high content of β -sheets structure within the SF matrix may induce the adsorption of some peptides, resulting in potential toxicities and inflammation *in vivo* [28].

Likewise, antiseptic drug-loading and release behaviors highly depend on secondary structure of SF, which further guide the antibacterial and osteoinductive performances [29]. Speculatively, varying secondary structures of SF would induce alterations of AgNPs in diameters and morphologies during the in-situ reduction process. As proved, the concentration and morphology of Ag-NPs played a vital role in promoting osteogenic differentiation of urine-derived stem cells at a suitable concentration [30,31], and the size-dependent antimicrobial and cytotoxic properties of silver nanoparticles were also stated [14,32]. Hence, it can be concluded a strong significance of tuning secondary structures to regulate the biological performances of drug-loaded SF coatings. However, to the best of our knowledge, none of the studies clearly elucidates the influence of varying secondary structures on the properties of such coatings. The secondary structures and conformations of SF could be flexibly modulated by some external conditions, such as pH [33]. In detail, strong inter-chain aggregations can be evoked by an increase of hydrophilic groups at low pH, while the conformation tend to be stretched due to the repulsion of charged carboxyl groups at high pH [14,34].

In the present study, we investigate SF-based coatings with varying secondary structures and components to address five main goals: (1) to prepare and characterize AgNPs/Gen-loaded SF coatings with varying secondary structures and components; (2) to compare the antibacterial and biocompatible performances of different SF-based coatings *in vitro*; (3) to evaluate the immune responses of these SF-based coatings after the subcutaneous implantation for 1 month; (4) to verify the feasibility and flexibility of this functional coating applied to complicated geometries; (5) to assess the *in vivo* osteoinductive ability of these bioactive interfaces in a rabbit femoral defect model. This work intended to help guiding a better understand and design of the antibacterial and osseointegrated coatings for bone implants.

2. Experimental section

2.1. Preparation of AgNPs/gen-loaded SF coatings with varying secondary structure

The *B. mori* silk was dissolved in established process and purified by removing the sericin to gain SF fraction, described in our previous study [12]. The final SF was ready to use in 5 wt% water solution.

Before reducing Ag⁺, the pH of SF solution was adjusted to 3.5, 6 and 9.5 by 1 M HCl or NaOH. Then, AgNO₃ powders (40.0–80.0 mg) and Gen powders (0.4 – 2.4 g) were mixed with 6 mL of 5 wt% SF solution, forming a translucent AgNO₃/Gen/SF mixture solution. The final AgNO₃ and Gen concentration in the mixture were 2 mM and 1 mg/mL, respectively. Then, the mixture solution was exposed to UV irradiation (Sankyo Denki, GL4; 254 nm; $T=25~^{\circ}$ C) for 2 h, and the final AgNPs/Gen/SF solution was stored at 4 °C for further use.

Commercially pure wrought titanium (cp-Ti) plates (99.9 mass% Ti, $10 \times 10 \times 0.5$ mm, Suzhou electronic material co.,LTD) were polished by 2000 grit and rinsed with ultrasonication in acetone, ethanol, and deionized water (DI) to get spotless and dehydrated surfaces, following by constructed with polydopamine (PD) layer and SF-based coating. In brief, cTi discs were placed into 2 mg/mL dopamine hydrochloride (Alfa Aesar) with Tris-HCl buffer (10 mM, pH = 8.5; Sigma) for 24 h while constantly vibrating in the dark at 37 °C, and then the excess monomer and particles were removed by thorough ultrasonication in Tris-HCl buffer [35]. Then, these Ti-PD discs were immersed with 10 μ L AgNO3/Gen/SF solution, following by evaporation at 30 °C and 60 °C to form functional coatings with varying structures and compositions.

2.2. Morphological and chemical characterization

Ag nanoparticles was investigated by transmission electron microscopy (TEM, H-9000, Hitachi) under an operating voltage of 100 kV. Briefly, AgNPs/Gen/SF mixture solution was diluted by DI water and dispersed by ultrasonic waves, then dropped onto carbon-coated copper grids, air-dried before observation. UV-visible spectra were recorded as a function of the reaction time on a UV-1601PC spectrophotometer (Shimadzu, Japan) operated at a resolution of 1 nm. The particle size distribution of Ag-NPs was evaluated using dynamic light scattering (DLS) measurements, three samples per group and three times testes per sample. Intensity-time autocorrelation functions were measured with acquisition times of 15 s for 10–20 min at a scattering angle of 90°.

The characteristic functional groups of SF-based coatings were identified by Fourier Transform Infrared (FTIR) microspectroscopy (Nicolet 750, USA), with a wave number ranging from 400 to –4000 cm⁻¹. With the help of Peak Fit 8.0 software, Fourier self-deconvolution (FSD) method was used to analyze the amide I (1600–1700 cm⁻¹) peak of each coating. At the same time, Origin 9.0 software was used to curve-fit the FSD spectrum, and Gaussian curve was curve-fitted. The peak assignment of the amide I region was as described in the literature [33]. At least three samples of each coating prepared independently, was analyzed.

In addition, the composition and element states of the samples were characterized by X-ray photoelectron spectroscopy (XPS; AXIS Ultra, Kratos Analytical Ltd.), and the binding energy was calibrated by the C 1s hydrocarbon peak at 284.8 eV. Quantitative analysis was performed with the help of Casa XPS software.

The surface morphology of SF-based coating was observed using field-emission scanning electron microscopy (FESEM, S-4800, Hitachi). To improve electrical conductivity, the coatings were first sputtered with gold, and then observed at an accelerating voltage of 5 kV. Further, five area from SEM images were randomly selected to measure the average diameter of AgNPs forming at different conditions by ImageJ software.

The crystalline phase of AgNPs and the β -sheet structure of SF were characterized by X-ray diffraction (XRD), the copper target was used as the radiation source ($\lambda = 1.540598 \text{Å}$), and the working voltage was 40 kV. Set the different angles (2θ) in increments of 10 to 90° with a step size of 4 min^{-1} .

2.3. Wettability and protein adsorption

The hydrophilicity of the SF coating was measured by a contact angle goniometer (SL200B, Kono, USA). Place the sample on the cover glass, and randomly drop five DW droplets on different positions for measurement.

FITC-labeled bovine serum albumin (FITC-BSA, 100 μ g/mL, Sigma) was co-cultured with SF-based coating for 1 hour at 37 °C for protein adsorption experiments [36].

In order to quantitatively calculate the amount of protein adsorbed on the SF coating, the supernatant was collected after the co-incubation and measured with a multi-label reader (2300, Perkin Eimer) at an excitation wavelength of 488 nm and an emission wavelength of 525 nm. According to a series of FITC-BSA solutions of known concentration, the absorption of BSA was calculated according to the standard curve. Then, the sample surface was cleaned with PBS, and the attached protein was observed under a laser scanning confocal microscope (LSCM, Carl Zeiss, Germany).

2.4. Ion release

Samples (n=3) were submersed in phosphate buffer solution (PBS, pH = 7.4) at 37 °C under static conditions. At predetermined times, the leaching medium was collected and freshly added. Analysis was performed by using inductively coupled plasma mass spectrometry (ICP-MS; Agilent 7700 \times , U.S.). Besides, the total Ag content per sample was determined similarly after dissolving the particles in HNO₃ (n=3).

2.5. In vitro antibacterial experiments

A model *S. aureus* mutans (ATCC 25923), which was closely related to most orthopedic infections, was utilized to co-culture with samples in the Luria Bertani (LB) medium at 37 °C to assess the antibacterial activity of the SF coatings (n=3). Before bactericidal experiment, all sample surfaces were sterilized by UV irradiation for 2 h, then immersed in 500 mL bacterial suspension with a presupposed concentration (OD₆₀₀ ~0.5, corresponding to ~2 × 10^8 colony forming units (CFU)/mL) in aerobic conditions for 6 h and 24 h for anti-attachment assay, and 7 d for anti-biofilm assay.

Subsequently, in order to evaluate the coating's ability to inhibit bacterial adhesion, the WST-8 kit (Dojindo, Kumamoto, Japan) was used to test the bacterial viability according to the manufacturer's instructions. In detail, after 6 h coculture with 2 mL *S. aureus* (2 × 10⁸), the bacteria on the surface and in the suspension were collected and mixed with WST-8 (containing electron mediator) as a ration 10:1. After half hour reaction, the color of solution turned into deep yellow, and in the presence of WST-8 and electron mediators, colorimetric measurement of formazan dye produced during microbial metabolism could indirectly reflect the number of bacteria. The naked sample was used as a reference to eliminate the influence of the background.

Then, the surface of the sample was washed with sterile PBS to remove non-adherent bacteria, and then fixed with 4% glutaraldehyde. For each sample, at least 5 random low-magnification and high-magnification SEM images were taken to count the number of attached bacteria and observe their morphological changes. In addition, the Live/Dead®BacLightTM bacterial viability kit (Molecular ProbesTM, Invitrogen) was used to perform fluorescent staining to distinguish dead/live bacteria and visually observe the formation of biofilms. The kit contained two dyes, SYTOTM9 And propidium iodide (PI). Because of their different ability to penetrate bacterial membranes, PI only targeted ruptured cell membranes, while SYTO could penetrate complete membranes [37]. After washing with 0.85% saline, 500 mL of SYTO (6 mM) and PI (30 mM) staining reagent mixture were added to the surface of each sample. After staining for 15 minutes in a dark environment, five locations were randomly selected for observation under a confocal laser scanning microscope (CLSM), and finally quantitative data analysis was performed with Image J software.

After 7 d of co-cultivation between the sample and the bacteria, the surface was washed with PBS to remove the bacteria that did not adhere firmly, and the back of the sample was carefully

cleaned with a swab soaked in 70% (v/v) EtOH. To observe the formation of biofilm, the sample was fixed with 4% PFA, stained with 0.1% (w/v) crystal violet for 15 minutes, and then washed with PBS 3 times to remove unbound dye. After the photo was taken, the dye was eluted with 95% (v/v) EtOH, and its absorbance was measured at a wavelength of 570 nm.

According to the operating procedure, the formation of reactive oxygen species (ROS) was measured by the sensitive 2',7'-dichloro-fluororesin diacetate (DCFH-DA) fluorescent agent. Incubate the dilute DCFH-DA dilution (non-fluorescent) with bacteria (on the sample's surface) for 2 h at 37 °C. In the ROS environment, it was converted to 2',7'-dichlorofluororescin (DCF, fluorescence). CLSM fluorescence images were observed at 488 (Ex) and 535 (Em) nm, and five random areas were selected for each sample for observation. Image J software was used for quantitative data analysis.

2.6. In vitro biocompatible and osteogenic assessment

2.6.1. Cell culture and seeding

The mouse preosteoblast MC3T3-E1 cells were fostered in α -MEM medium containing10% fetal bovine serum (FBS) and 1% penicillin/streptomycin in a humidified incubator with 5% CO $_2$ at 37 °C.

2.6.2. Cell adhesion

SEM observations and polychrome immunofluorescence staining were utilized to visualize the initial attachment and spreading. After 6 h of cultivation, samples were rinsed twice with PBS and fixed in glutaraldehyde (2.5%) for 2 h. Subsequently, the fixed cells were rinsed again and dehydrated with graded concentrations of ethanol (30–100%). After complete dry at room temperature (RT), the samples were coated by gold-sputtering and observed under SEM. For immunofluorescence staining, the washed cells were submerged in 5 μ g/mL fluorescein diacetate (FDA) solution for 5 min. Later, cells were rinsed with PBS and visualized under confocal microscopy. The quantitative results were analyzed by Image J.

2.6.3. Cell proliferation and morphology

Depending on the mitochondrial measurement, Cell Counting Kits (CCK-8, Dojindo) was employed to assess cell activity and proliferation, as previous reported [12]. Besides, the cell attachment and spreading were stained by fluorescent dye and visualized under CLSM. In brief, through rinsing three times with PBS and fixing in 4% PFA, the settled cells were permeabilized and counterstained with FITC-phalloidin (1:200, 40 min; Sigma) and DAPI (1:1000, 5 min).

2.6.4. Cellular live/dead staining

The survival capacities of MC3T3-E1 cells on different coatings was assessed by staining living cells with 2 μ M Calcein AM and the dead cells with 4 μ M PI (Live/Dead Cell Stains, Dojindo, Kumamoto, Japan), following as the operation manual. After that, the living and dead cells were observed by confocal microscopy according with green and red, respectively.

2.6.5. Cell apoptosis and intracellular ROS levels

To assess the cytotoxicity of samples, an LDH kit (Abcam, Cambridge, MA) was used to measure the extracellular release of lactate dehydrogenase (LDH), closely related to cell apoptosis. Following the manufacturer's protocol, LDH value at the single-cell level (i.e., cellular LDH activity) was revealed by standardizing the total LDH activity to the number of cells. As depicted in antibacterial experiment, a DCFH-DA-labeled fluorescence probe was used to assay the levels of intracellular ROS in MC3T3-E1 cells caused by SF-based coatings.

2.6.6. Extracellular matrix (ECM) collagen and calcium assays

After culture for 28 d, ECM collagen and calcium salts expressed by MC3T3-E1 cells was specifically stained by histochemical dyes Sirius Red (SR, 0.1%; Sigma) and Alizarin Red S (ARS, 2%; Sigma), respectively. In short, cells cultured on surfaces were fixed in 4% PFA and rinsed with PBS, then incubated with 500 μL of SR or ARS dye solution for 18 h or 15 min, respectively. Next, the resultant surfaces was thoroughly washed by acetic acid solution (0.1 M) and DI water, after that, they were completely dried and photographed. Quantitatively, dyes were extracted using 50% 0.2 M NaOH/methanol (for SR) and 10% cetylpyridinium chloride (for ARS), and the samples were then read on a microplate at 570 or 562 nm.

2.6.7. Alkaline phosphatase (ALP) activity

Osteogenic differentiation of MC3T3-E1 cells were assessed by cultivating in osteogenic differentiation media. Mature cells (>70%) were collected and cultured with sterilized samples at a density of 1×10^5 cells/mL in 24-well tissue culture plates. The media were changed every other day. After incubation for 7 and 14 days, an ALP assay kit (Nanjing Jiancheng, China) was utilized to analyze intracellular release of alkaline phosphatase (ALP). In brief, cells cultured on surfaces were cleaned with PBS and lysed with 1% Triton X-100 for 1 h. Next, the cell lysis was transferred to 96-well plate with 20 µL/well and mixed with the working solution following the manufacturer's instruction. After complete colorimetric reaction, the absorbance of mixed solution was tested by a plate reader at 520 nm. The final data were normalized by the total protein amount, determined by BCA assay kit. To visualize the ALP expression on the surfaces, BCIP/NBT ALP color development kit (Beyotime, China) was used to stain the cells with deep blue color.

2.6.8. Real-time polymerase chain reaction (RT-PCR)

According to the instructions in the operating manual, after 7 and 14 days of co-cultivation with the sample, the total RNA of the cells was separated using Trizol reagent (Sigma) and reversed using the RevertAid First Stand cDNA synthesis kit (Fementas, Vilnius, Lithuania) record. After that, SYBR Green PCR Master Mix was used to perform RT-PCR using the ABI PRISM 7500 Sequence Detection System (Applied Biosystems, California, USA). The housekeeping gene was glyceraldehyde-3-phosphate dehydrogenase (GAPDH). The primers used in this study were: shorty-related transcription factor 2 (Runx2), (forward) 5'-AG-GAATGCGCCCTAAATCACT-3' and (reverse) 5'-ACCCAGAAGG-CACAGACAGAAG-3'; type I collagen alpha 1 (Col1a1), (forward) 5'-AAGAAGCACGTCTGGTTTGGAG-3' and (reverse) 5'-GGTCCATGTAGGCTACGCTGTT-3'; osteocalcin (°CN), (forward) 5'-TTTCTGCTCACTCTGCTGACC-3' and (reverse) 5'-CAGCACAACTCCTTCCTACCA-3'; ALP, (forward) 5'-TCGGGACTGGTA CTCGGATAAC-3' and (reverse) 5'-GTTCAGTGCGGTTCCAGACATAG -3'. The cycle threshold (Ct value) was selected, and the multiple difference was determined by the $\Delta\Delta$ Ct method. The untreated cells in the normal growth medium were used as the control

2.7. In vivo experiments

2.7.1. In vivo implantation and fluorescent labeling

Rabbit femoral defect model was used to assess the *in vivo* osseointegration ability of SF coating. In brief, 16 groups of the porous Ti64 scaffolds, including untreated and SF coating-treated implants, were inserted in the bilateral femur defects of 16 mature male New Zealand rabbits. Ketamine (50 mg/kg) was utilized to anesthetize the rabbits by intramuscular injection. After sterilizing skin with 0.5% povidone iodine, the bone defects were surgically opened. A 5 mm diameter drill was used to perforate femur along with saline wash, and then the scaffold was implanted in the bone

defect by push mounting. The opening was sutured by absorbable thread (PDS II, Ethicon, USA) in layers. 0.1 g/kg penicillin was intramuscularly injected in rabbits for 3 days postoperatively. To observe the new bone regeneration process in the implants after the embedding, new-generated bone was labeled by *in vivo* sequential fluorescent labeling at different time points. Commonly, subcutaneous injection of calcein green (10 mg/kg, Sigma, U.S.A.) and tetracycline (30 mg/kg, Sigma, U.S.A.) was carried out at 3 and 7 weeks post-embedding, respectively. After 8 weeks feeding, all the rabbits were euthanized and the intact tissues containing scaffolds were taken out. All the experimental protocols were approved by the Institutional Animal Ethics Committee of Peking University, and all rabbits were raised following the national guidelines for care and use of laboratory animals.

2.7.2. Histological evaluation

After soaking in 10% formalin, specimens were dehydrated with gradient ethanol solution (40-100%), and then the internal implant was carefully removed and immersed in paraffin wax. Prepare five histological cross-sections (6 mm thick) of each sample, stain them with hematoxylin-Illinoin (H-E), and take pictures under a fluorescence microscope (DP71, Olympus) to observe the inflammation of the subcutaneous tissue. ImageJ software was used to analyze the images, and the thickness of the fibrotic capsule around the implant and the number of fibroblasts were quantitatively calculated.

2.7.3. Micro-CT analysis

Rabbit femurs were retrieved and scanned by using a self-built micro-CT device (InveonTM, Siemens Medical Solutions U.S.A., Inc.) at a spatial resolution of 9 μm and a scanning rate of 6°/min. The X-ray source voltage was 80 kV and beam current was 80 mA using filtered Bremsstrahlung radiation. Three-dimensional (3D) reconstruction was performed using Inveon Acquisition Workplace. The new-generated bone was separated from soft tissue and implant by partition of different Hounsfield units (HU), in the range from 1000 to 2250 HU. The% bone volume (BV/TV) was defined as the ratio of bone volume to the total volume of the region.

2.7.4. Histological examination

After 8 weeks of implantation, the intact tissue containing scaffolds were excised for fluorescence and histological analysis. All samples were fixed in 10% formalin for 14 days, and dehydrated in serial concentrations of ethanol (70%, 85%, 95%, and 100%) for 3 days each, following with embedding in methyl methacrylate and cutting by an EXAKT system (EXAKT Apparatebau, Norderstedt, Germany). Fluorescent microscope was employed to analyze the stained samples. Generally, the new-born bone at the third and seventh week were labeled by a green calcein and an orange tetracycline, respectively. In addition, the sections from another samples were stained with methyl blue and basic fuchsin, showing red color. An Image-Pro-Plus software was utilized to quantitatively analyze the bone in-growth (BI) and bone-implant contact ratio (BICR) according to 2 middle longitudinal sections of each areas. The BI was defined as the percentage of new bone within the scaffold. The BICR was measured as the faction of the surface area of the implant in contact with the bone.

2.8. Statistical analysis

For all experiments, values for statistical analysis were reported as Mean \pm SD. An independent-sample *t*-test was performed to test the significant differences regarding the *in vitro* results, whereas the significant differences of the *in vivo* results

were determined by a nonparametric test (Mann–Whitney) using SPSS (17.0 version). P < 0.05 was considered statistically significant.

3. Results and discussion

3.1. A one-step assembly of SF-AgNPs-Gen colloidal solution

As shown in Fig. 1a, the morphology and size changes of AgNPs reduced under different pH conditions could be clearly observed through TEM images. Most AgNPs showed irregular granular or globose morphology. By analyzing 50 nanoparticles, the average diameter of AgNPs reduced under different pH conditions were calculated, 53.4 \pm 2.7 nm (pH 3.5), 36.7 \pm 3.2 nm (pH 6) and 18.6 ± 2.7 nm (pH 9.5). Notably, with the increase of pH value, the particle size of AgNPs decreased significantly. During the reduction process of Ag+, some SF molecular chains would wrap AgNPs through protein-metal interactions to achieve the purpose of stabilizing AgNPs and preventing agglomeration, so AgNPs could uniformly distributed in the SF solution for a long time. There were also some SF molecular chains that self-assemble to form larger SF nanomicelles (about 50 nm). Fig. 1c showed the UV-vis of the SF-AgNPs-Gen colloidal solution. Initially, the SF-AgNPs-Gen solution was colorless. After UV irradiation for 2 h, the solution color changed to pale yellow and eventually dark brown as shown in Figure S1. The color change was caused by the surface plasmon resonance (SPR) of AgNPs. The SPR peak at 420 nm belonged to AgNPs, and a significant red shift occurred with the increase of pH value. In comparison, the characteristic peak intensity of Ag-NPs obtained under acidic conditions (pH = 3.5) was significantly higher than that of neutral and alkaline, which was attributed to the larger particle size of AgNPs under acidic conditions. The absorption peak at $\lambda = 275$ nm was the characteristic peak of SF, mainly due to the presence of amino acid end groups such as Tyr, Phe, and Try in the SF chain [38]. Under acidic conditions, the shift of the characteristic peaks of SF to high wavelengths is due to the protonation of amino acid end groups in the SF molecular chain. DLS analysis confirmed that at pH 3.5, the particle size distribution of AgNPs was mainly concentrated at 55 \pm 6 nm (Polydispersity Index 0.18), and the existence of a small peak with a small particle size was due to insufficient reduction (Fig. 1d). At pH = 9.5, only one characteristic peak was observed in the particle size distribution of AgNPs, with an average value of 20 \pm 2 nm (Polydispersity Index 0.12). In contrast, the main peak at pH 6 was located at 40 ± 3 nm (Polydispersity Index 0.25) and the distribution was wider, which means that the particle size of AgNPs obtained under neutral conditions was more dispersed. However, it is worth noting that the diameter detected by DLS is the hydrated diameter, which is usually larger than the true diameter of the nanoparticles.

Fig. 1b illustrated the formation mechanism of AgNPs at different pH conditions. When the pH was 3.5, the hydrophobic and uncharged carboxyl groups in the SF molecular chain would increase, leading to obvious interchain aggregation, hindering the electrostatic attraction of the tyrosine (Tyr) and Ag⁺, and the contact probability between Tyr-and Ag⁺ would be significantly reduced. Moreover, due to the protonation of amino acids, the positively charged Gen (isoelectric point, 5.7 \pm 0.2) competed with Ag $^+$ for electrostatic binding with Tyr, resulting in insufficient reduction sites and reduced reduction efficiency. Therefore, AgNPs displayed the largest diameter (55 nm) under acidic conditions. Under alkaline conditions (pH = 9.5), due to the increase of hydrophilic groups and negatively charged groups, the SF molecular chains repelled each other, the conformation stretched, and the contact sites of Tyr-and Ag+ were more numerous and reduction efficient were more intense. As confirmed, Gen can acted as a bridge between SF

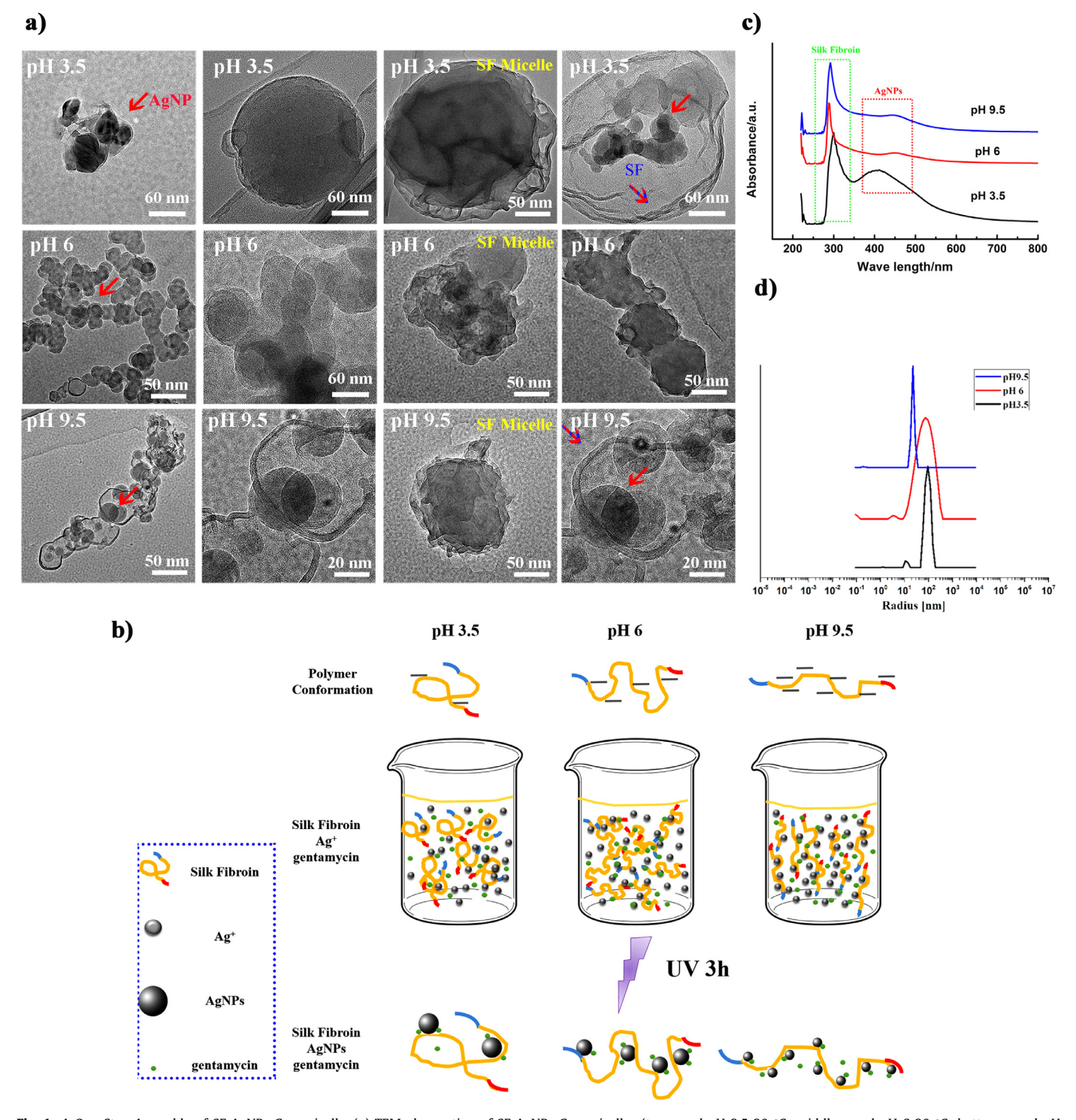


Fig. 1. A One-Step Assembly of SF-AgNPs-Gen micelle. (a) TEM observation of SF-AgNPs-Gen micelles (top panel pH 3.5 30 °C; middle panel pH 6 30 °C; bottom panel pH 9.5 30 °C); (b) formation mechanism of AgNPs; (c) UV-vis spectra and (d) dynamic light scattering (DLS) of the synthesized SF-AgNPs-Gen.

and AgNPs, and improved the reduction efficiency of SF at pH> 5.7 [12]. Also, temperature rise could lead to aggregation of AgNPs.

3.2. Characterization of SF-based coating

As shown in Fig. 2, AgNPs were evenly distributed in the SF-based coating, the coating was flat and dense, and the surface roughness was relatively low. In contrast, as the pH value increases, the particle size of AgNPs became smaller and the distribution became more uniform. This agreed with the TEM images of

AgNPs at different pH conditions (Fig. 1a). In addition, the increase in temperature caused agglomeration of AgNPs, and the diameter of the particles increased significantly.

Characteristic functional groups and microstructures of different SF-based coating surfaces were characterized by FTIR. Obviously, both the decrease in pH and the increase in temperature could promote the SF I-type structure (α -helices) to the II-type structure (β -sheets). As shown in Fig. 3b, the characteristic peaks of SF-based coatings under different conditions basically overlapped, meaning that they contained the same secondary structure, but the

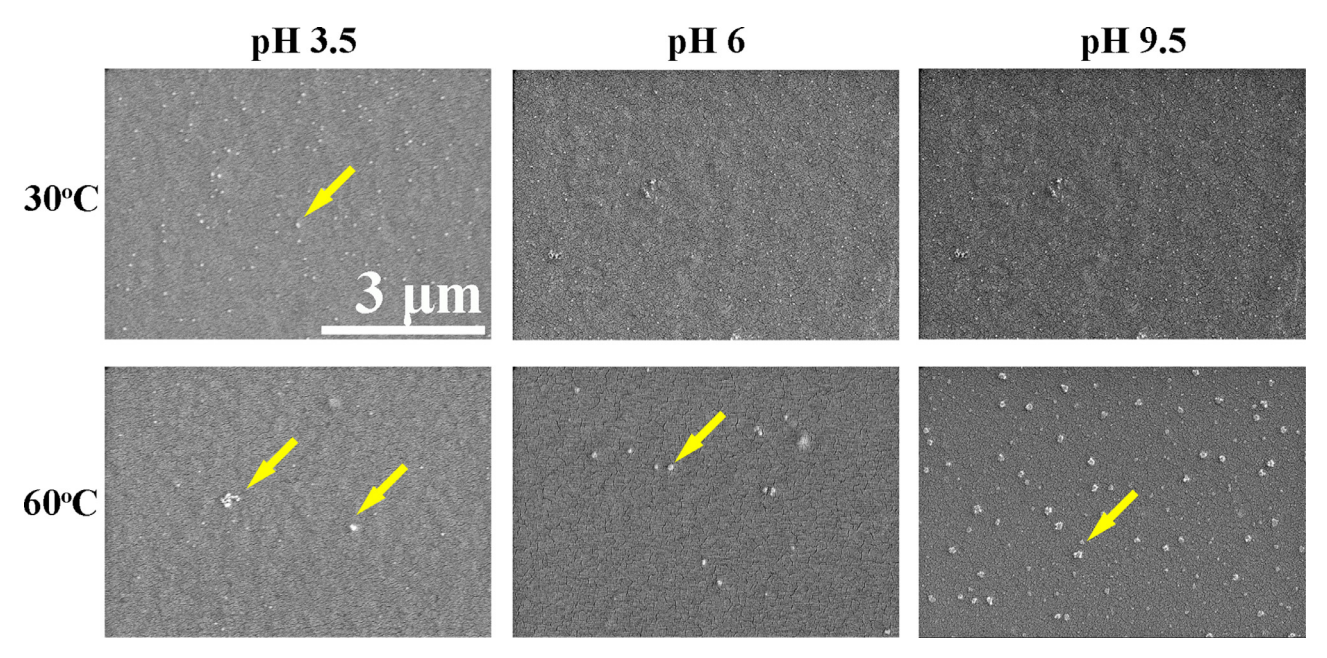


Fig. 2. SEM images of AgNPs/Gen/SF composited coating which were dried at 30 °C and 60 °C.

red shift and intensity changes of the peaks represented different contents of α -helices and β -sheets structure. In contrast, when the pH value was 3.5, the characteristic peak (1634 cm^{-1}) of the lphahelices structure turned into a characteristic peak (1617 cm⁻¹) of the β -sheet structure [39], which was attributed to acidic conditions inducing deprotonation of the carboxyl group and protonation of the amino group, leading to a conformational change in the SF molecular chain. The characteristic peak of the α -helices structure at 1531 cm⁻¹ disappeared, and only the characteristic peak of 1513 cm⁻¹ belonging to the β -sheet structure was observed in the amide II region [39]. In addition, the characteristic peak at 1233 cm⁻¹ in the amide III region (random coil structure) also shifted to 1230 cm⁻¹ (β -sheet structure) [40], which meant that the SF disordered structure reassembled into a layered crystal structure. On the other hand, temperature could also cause the transformation of SF secondary structure. As confirmed, both temperature increase and pH decrease could lead to the transformation of α -helices structure and random coil structure to β -sheet structure in SF-based coatings. In other words, the content of β -sheet structure in SF-based coatings could be controlled by adjusting pH and temperature. It was worth noting that the characteristic peak at 1623 cm⁻¹ was related to the carbonyl (C=O) tensile vibration

[41], indicating that the phenolic hydroxyl group (-OH) of the Tyrwas oxidized and converted into a C=O group, which was intuitive evidence that SF reduced Ag⁺ to AgNPs. In detail, the peak structure Fourier self-deconvolution (FSD) was used to determine the secondary structure content (random coil, α -helices, β -sheet) of SF-based coatings prepared under different conditions. The FSD spectrum of three characteristic coatings were shown in Fig. 3c: m (β -sheet structure 28.3%, pH 6, 30 °C), α (β -sheet structure 19.0%, pH 9.5, 30 °C) and β (β -sheet structure 41.0%, pH 3.5, 60 °C). Table 1 summarized the secondary structure content of different SF-based coatings. According to FTIR and FSD spectra, β -structured coating had the highest β -sheet structure content (41%), while α -structured coating had the highest α -helices content (32.7%).

XRD further studied the changes in the crystal structure of the SF-based coating. Two different characteristic peaks corresponded to the silk fibroin I structure (12.2°, amorphous) and silk fibroin II structure (20.7°, crystalline). Obviously, all coatings contained both two structures. As the pH decreases, the characteristic peak at 20.7° increased, indicating that the silk fibroin II structure became dominant (Fig. 3d), confirming the effect of pH and temperature adjustment on the crystal structure of the SF-based coating, which is basically consistent with the FTIR data.

Table 1Content of secondary structure of SF at different condition (gray was at 30 °C, white was at 60 °C).

| рН | β-sheets (±2.4%) | randomcoils (±2.1%) | α-helices (±1.8%) | turns (±2.4%) |
|-----|------------------|---------------------|-------------------|---------------|
| 3.5 | 31.9 | 23.8 | 29.1 | 15.3 |
| 6 | 28.3 | 24.5 | 23.4 | 23.8 |
| 9.5 | 19.0 | 17.3 | 23.7 | 31.0 |
| 3.5 | 41.0 | 21.4 | 19.4 | 18.2 |
| 6 | 31.0 | 24.1 | 27.2 | 17.8 |
| 9.5 | 24.7 | 29.1 | 31.7 | 14.5 |

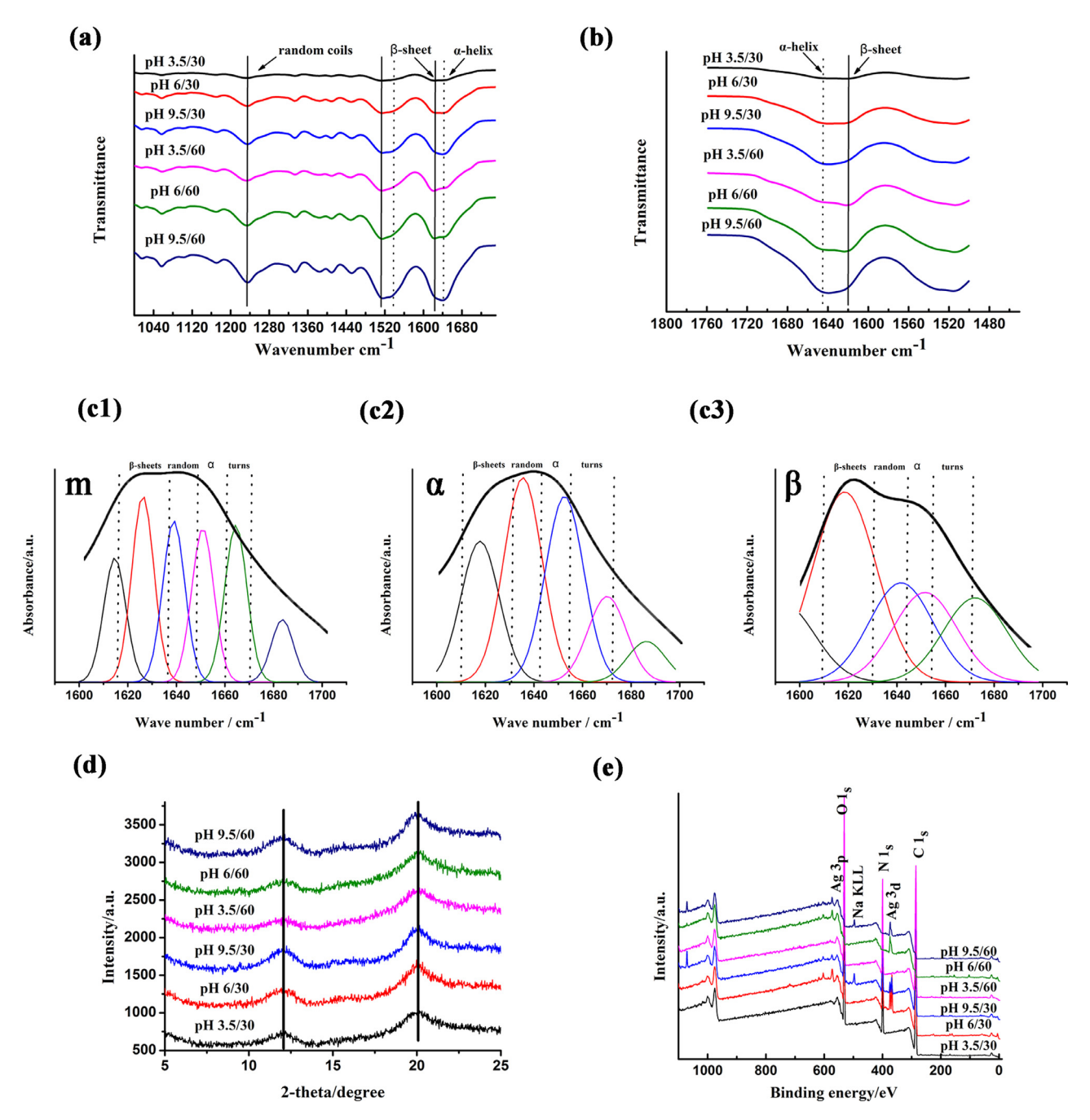


Fig. 3. Analysis of chemical composition for the SF-based coatings. (a) Micro-FTIR spectra; (b) magnified spectra of the specific area in image a; (c) absorbance spectra, amide I, deduced after Fourier self-deconvolution of pH 6 30 °C (c1), pH 9.5 30 °C (c2) and pH 3.5 60 °C (c3); (d) XRD patterns and (e) survey spectra of XPS.

The chemical properties and chemical bonds of the SF-based coatings were determined by X-ray photoelectron spectroscopy (XPS). All SF-based coatings' XPS spectra displayed three superstrong peaks, located at 284, 398, and 532 eV, which belong to C1, N1, and O1, respectively. Also, the C1s spectrum could be deconvoluted into four secondary peaks, namely C-C/C=C, C-O (H)/C-N, C=O/N-C=O and O=C-O (Fig. S2). However, due to differences in forming pH and temperature, the ratio of the secondary peaks was different. In the XPS spectrum of Ag3d (Fig. S2), the characteristic peaks of Ag (3d_{3/2}) and Ag (3d_{5/2}) of the SF-based coating prepared at pH 6 and 9.5 were 374.1 eV and 368.1 eV, respectively, indicating that AgNPs were metallic and uniformly distributed, which matched well with JCPDS card No. 04-0783 (Fig. S3). In addition, no Ag (3d) characteristic peak was observed in the SF-based coat-

ing prepared at pH 3.5, which was attributed to the large particle size of the agglomerated particles with changed crystal structure. The chemical stability of AgNPs/Gen-loaded SF-based coatings stemmed from the stabilizing effect of SF on AgNPs and the protection of bactericides' activity. Also, by controlling the forming steps and conditions (pH and tempreture) consistent, the coatings (one kind) from different batches had the same characteristics *e.g.* the size of particles and the structure.

3.3. Wettability and protein adsorption

When it comes to the surface modification of biomaterials, the surface wettability should be studied in depth, because it exerts a crucial effect on the initial protein adsorption and further

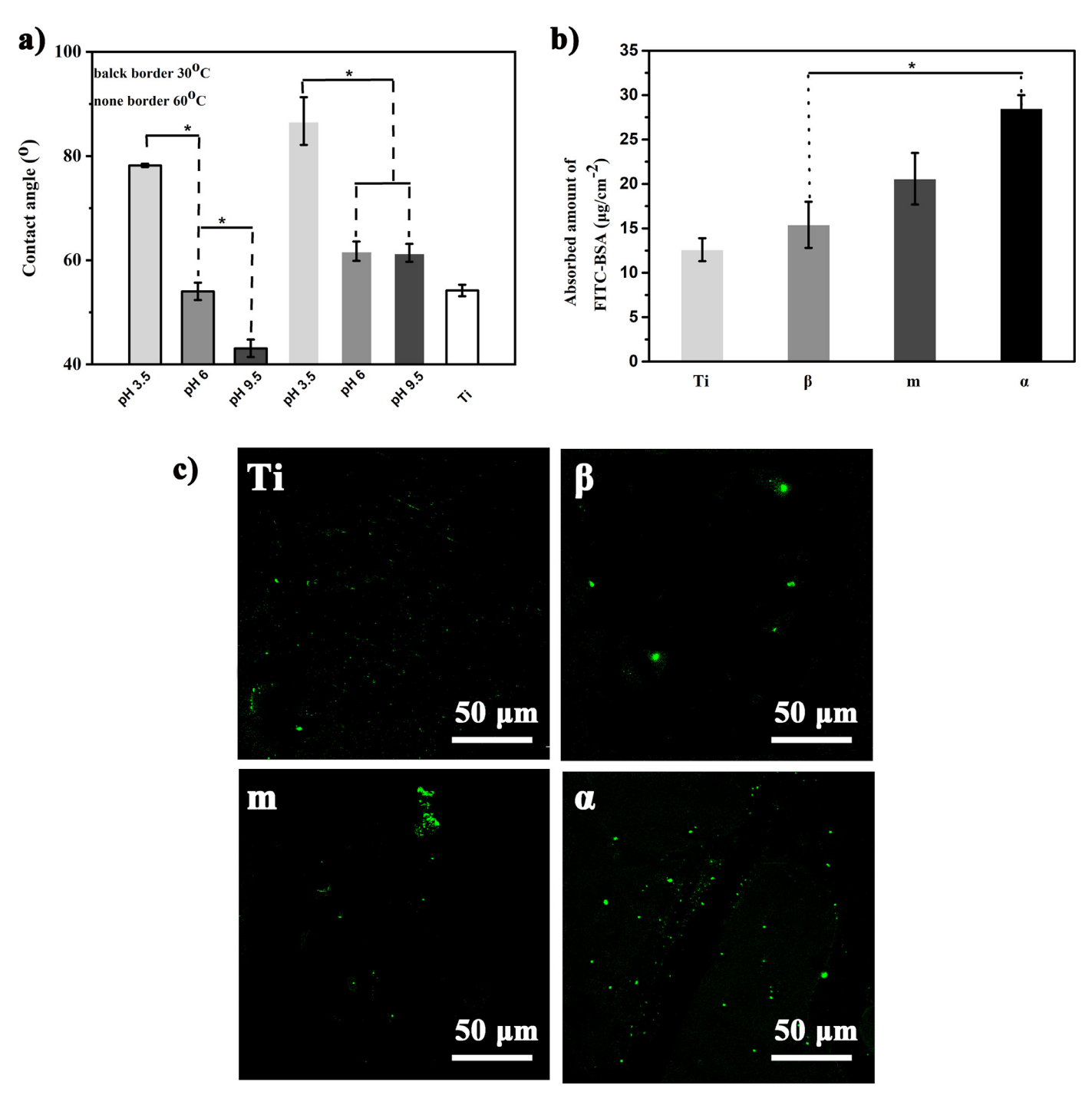


Fig. 4. Surface properties of different samples: (a) hydrophilicity and (b, c) protein adsorption.

cell adhesion. Therefore, the hydrophilicity of the SF-based coatings' surface was measured by the contact angle (CA) method (Fig. 4a). As a commonly used hard tissue implant material, Ti was relatively hydrophobic (53.2 \pm 3.8°). In comparison, the SF-based coating (30±3.1°) formed at pH 3.5 was the most hydrophobic (78.2 \pm 5.2°), while the CA values of the m-structured coating (pH 6) and the α -structured coating (pH 9.5) had decreased by 24.2° and 35.1°, respectively. It means that α -structured coating was potentially biologically active. When discussing the effect of temperature, it could be observed that the increase in temperature at the same pH results in an increase of the CA of the SF-based coating by about 10°. One possible cause was the increase of β -sheet structure with hydrophobic segments at

high temperature, and the other was the agglomeration of AgNPs (Fig. 2).

When implants are implanted in the body, the first thing that occurs at the implant/tissue interface is protein adsorption, which rapidly forms a thin layer of protein, which has a critical impact on subsequent cellular behaviors such as adhesion, spreading, proliferation and differentiation [36]. The bioaffinity of SF-based coatings was evaluated by using non-specific FITC-labeled BSA. Specifically, the sample was incubated in a 1 mg/mL FITC-labeled BSA solution for 2 h, and the coating surface on which the BSA was adsorbed emitted green fluorescence at an excitation wavelength of 488 nm. As shown in Fig. 4c, due to the high content of the β -sheet structure, the fluorescence of

Table 2 The release rate of Ag^+ from different coatings at pH 4 and 7 conditions ($\mu g/h$).

| pН | pH pH 4 | | | pH 7 | | |
|-----------|--------------|--------------|--------------|--------------|--------------|--------------|
| Time | α | m | β | α | M | β |
| | (± 0.01) |
| 0-5 h | 49.720 | 31.412 | 60.661 | 10.921 | 11.381 | 13.852 |
| 5-24 h | 19.121 | 19.952 | 19.357 | 16.831 | 17.505 | 35.852 |
| 24-72 h | 0.218 | 1.811 | 0.033 | 0.042 | 0.298 | 0.101 |
| 72-144 h | 0.519 | 1.093 | 0.079 | 0.014 | 0.087 | 0.333 |
| 144-216 h | 0.155 | 0.518 | 0.019 | 0.024 | 0.031 | 0.008 |
| 216-408 h | 0.168 | 0.211 | 0.009 | 0.011 | 0.011 | 0.002 |

the β -structured coating was relatively dispersed, and some highintensity fluorescent aggregates were observed on the surface. In contrast, the α -structured coating surface exhibited uniform protein adsorption and showed stronger fluorescence levels. According to the quantitative data (Fig. 4b), the naked Ti showed poor protein adsorption, compared with that, the α -structured coating had the highest protein content (P < 0.05), which means that the α -structured coating could significantly improve the bioaffinity of Ti implants, which tended to adsorb various ECM proteins, such as fibronectin, glycoproteins, and growth factors, supporting further cell attachment, spreading, and proliferation behavior on the implant surface. The hydrophilic α -helices structure of SF has repeating amino acid sequences, so it contains many active sites, which can be linked to proteins through electrostatic and hydrogen bonds [42]. In addition, studies have confirmed that small-sized AgNPs can adsorb various cellular proteins including BSA [43]. These two factors could explain the superior bioaffinity of the α -structured coating.

3.4. pH-responsive release of Ag+

The in vitro release behavior of Ag+ from SF-based coatings showed that α -structured coatings could achieve long-term sustained release in PBS solution at pH 7. As shown in Table 2, at initial immersion stage (5–24 h), the Ag⁺ release rate of β -structure coating was over twice that of α -structured coating, meaning that α -helices structure could effectively suppress the initial burst release. Within the first 3 h, the cumulative release of α -structured coating was only 35.2%, the m-structure coating was 55.4%, and the β -structure coating was 70.2%, the difference was very large. As shown in the Inset of Fig. 5b, with the extension of immersion time (5–24 h), β -structured coatings showed relative high release amount (almost 700 μ g) compared with m- and α -structure coatings, which was not conducive to long-term antibacterial performance and easy caused drug resistance in bacteria (Fig. 5b). As verified [33], SF-based coatings with higher type II structure (β sheet structure) were not conducive to long-term sustained release of drugs, and most antibacterial agents would be released in the early stage. In contrast, all coatings showed similar release behavior under acidic conditions (pH 4), with initial burst release and long-term sustained release, indicating that acidity was a necessary condition to trigger the release of antimicrobial agents from SF-based coatings. As shown in Table 2, the release rate of α structured coating at pH 4 condition was almost five folds that of pH 7 condition, presenting obvious pH-responsive release performance. In summary, compared to β - and m-structured coatings, α -structured coatings exhibited the best pH response release of Ag^+ due to their higher α -helical structure content, which could achieve the targeted release of antibacterial agents (bacteria trigger). The relevant mechanism was explained as follows: (1) As shown in the TEM image, AgNPs in the α -structure coating have the smallest particle size (20 nm), the uniform distribution and the tightest binding to the SF molecular chain; (2) The content of α -helix structure in the α -structured coating was the highest. The coating had more negative charge due to the deprotonation of the carboxyl group, which could strengthen the complexation with AgNPs through hydrogen bonding and electrostatic interaction, which was beneficial to the long-term sustained release and pH response release of AgNPs.

3.5. Bacteria-triggered antibacterial performance

Individual bacteria adhered to the surface of the implant can develop into a complete biofilm, which can cause serious infections (such as osteomyelitis). Worse still, biofilm can encapsulate and protect bacteria from the attack of host's immune system or antibiotics, and it is difficult to remove it from the surface of the implant. Therefore, preventing the initial microbial attachment has become a key step in preventing surgical infection [44].

First, the mitochondrial activity of bacteria was measured by the WST test, thereby studying initial anti-adhesion and bactericidal capabilities of SF-based coatings with three characteristic structures. Because S.aureus (typical Gram-positive bacteria) is closely related to most orthopedic infections, S.aureus was used as a model bacteria to study the antibacterial ability of SF-based coatings. It is well known that the surface of bare Ti is biologically inert, with no ability to inhibit the adhesion of bacteria, and the incidence of infection is high. As shown in Fig. 6a, compared with the bare Ti, the three SF-based coatings significantly inhibited the adhesion of S.aureus, and the bacteriostatic rate exceeded 60%. Also, the SF-based coatings exhibited strong ability to kill planktonic bacteria, and the released fungicide could kill more than 90% of the planktonic bacteria. It was worth noting that the α -structured coating displayed the best anti-adhesion and bactericidal ability, followed by the β -structured coating, and the m-structured coating showed the worst antibacterial performances. To further study the long-term antibacterial (low concentration Ag+ release) performance of the SF-based coating, the S.aureus concentration on the surface and suspension was tested after soaking in PBS solution for 24 h. As shown in Fig. S4, after 24 h of immersion, only the α -structured coating still showed anti-adhesion and planktonic bacteria-killing capabilities, benefiting from the α -structured coating suppressing the initial burst release of Ag+ and the high synergetic antibacterial efficiency of smaller size AgNPs (about 20 nm). As shown in Fig. 5d, after immersed in PBS for 24 h, the m and β -structured coating released 56.2% and 72.5% of Ag⁺, compared with only 35.4% of the α -structured coating (~370 µg), showing an ability to suppress the initial burst release. This result proved that α -structured coating could achieve anti-adhesion and antibacterial

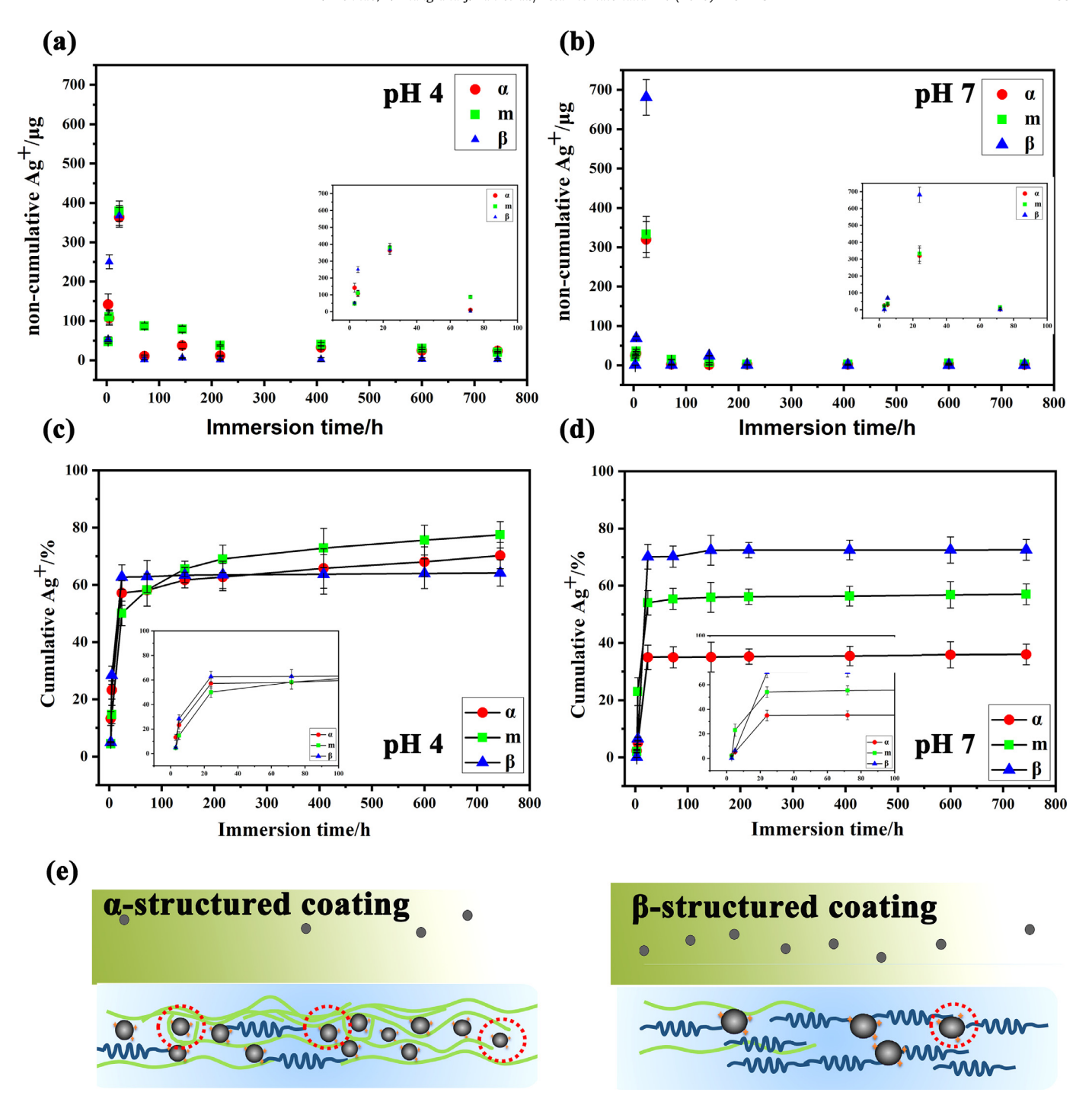


Fig. 5. Release behavior of silver in PBS. (a, b) noncumulative and (c, d) cumulative release curves of Ag+ after immersion at 37 °C for 30 days.

abilities under low Ag^+ release, and owned a long-term antibacterial ability.

In addition, the integrity of the bacterial cell membrane on the surfaces was observed by SEM, reflecting the damage effect on the bacterial membrane (Fig. 6c). Obviously, bacteria were easy to attach, reproduce, and gather on the surface of bare Ti, and mycoderm was spherical, intact, and vigorous. In contrast, α - and β -structured coatings caused bacterial membranes to wrinkle and damage, and the surface was heavily charged, which meant that the permeability of the bacterial membranes had changed. The m-structured coating showed the worst ability to destroy the bacterial membrane, and only a few broken bacterial fragments

were observed. In order to visualize the survival status of bacteria on the surface, Dead/Live staining fluorescence imaging was performed, as shown in Fig. 6d. Numerous live bacteria (green) could be clearly observed on the bare Ti surface, and they were vigorous and had the potential to form mature biofilms. In contrast, only a few, less active bacteria adhered to the surface of the m-structured coating, and even less *S.aureus* adhered to the surface of the β -structured coating, and most of them were death statue (red). In addition, the surface of the α -structured coating was clear and compact, which means that it had the strongest ability to inhibit bacterial adhesion and a self-cleaning ability.

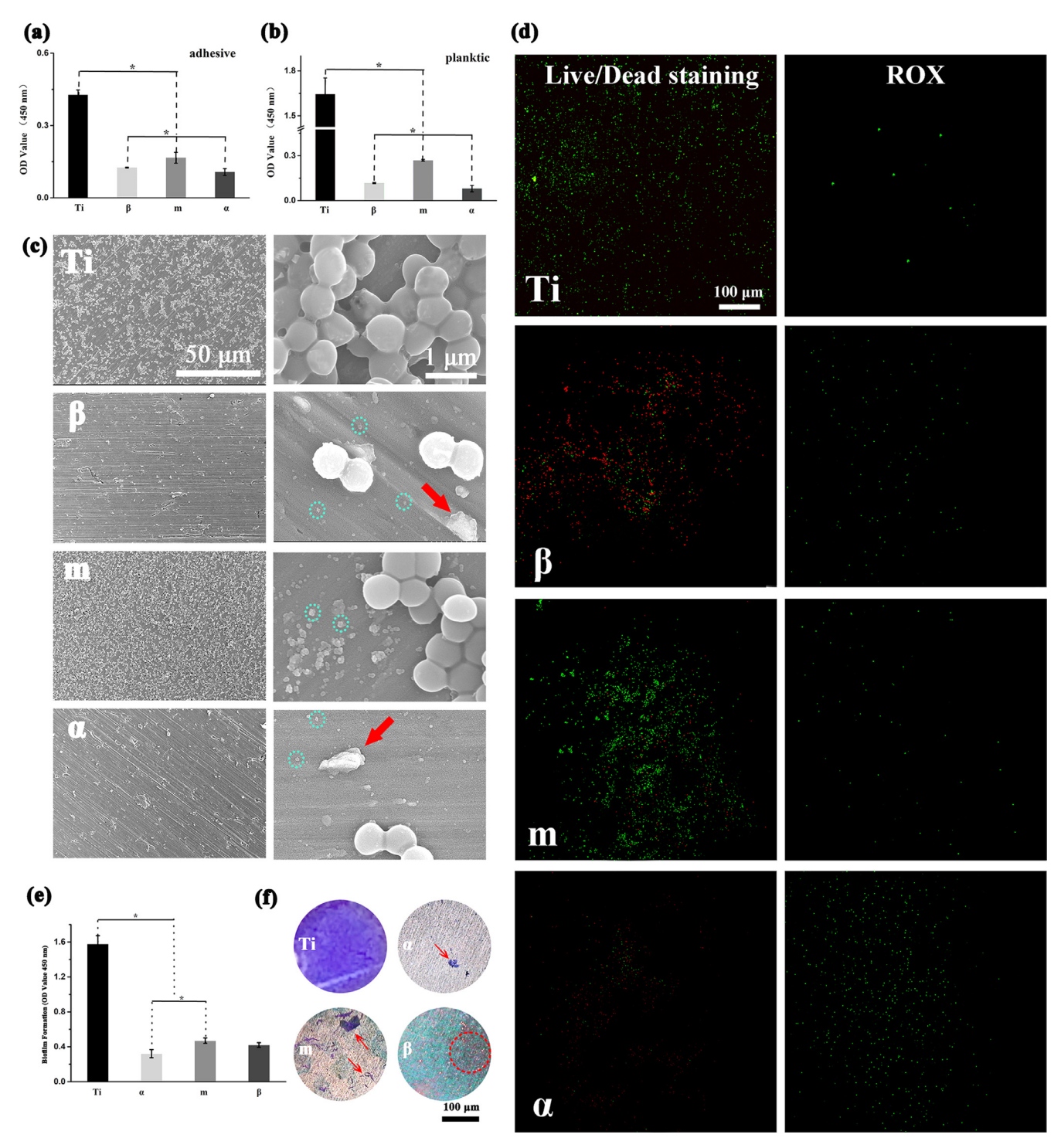


Fig. 6. Antibacterial activities of different samples against *S. aureus* (1×10^8 CFU/mL). (a) Relative adherence rate of bacteria; (b) planktonic bacteria-killing rate; (c) typical bacterial morphology; (d) Live/Dead staining and ROS qualitative results of the fluorescence densities; (e) biomass of adhered biofilms; (f) biofilm formation (visualized by crystal violet); patches of aggregate biofilms are indicated by circles.

For SF-based coatings, a possible antibacterial mechanism was the generation of excessive ROS, which could destroy the integrity of the bacterial membrane by affecting the respiratory chain reaction, finally leading to devitalization. Ag⁺ was highly related to the generation of ROS, targeting and interfering with the several cellular processes of bacteria *in vivo*. The DCFH-DA fluorescent probe was used to detect the oxidative stress caused by excessive ROS, and the fluorescence density was obtained by Image J software, as

shown in Fig. S5. Evidently, on the surface of the SF-based coating, especially the surface of the α -structured coating, the fluorescence density was significantly higher than that of the m- and β -structured coatings, which was consistent with the strongest fluorescence signal observed on the surface of the α -structured coating. This meant that bacteria-killing by excessive ROS generated was an important reason for the high-efficiency antibacterial ability of α -structured coating.

For the three SF-based coatings, the differences in microstructure played a vital role in topography, hydrophilicity, and drug release, and then influenced their antibacterial capabilities [45]. As reported [46], when the coating contained sharp nano-sized sheet structure, it could pierce the membrane of S.aureus to form localized nanopores. Sufficient amounts of multipoint pores could trigger the efflux of cytoplasmic components. From a similar viewpoint, we proposed one possible speculation, that due to high content β -sheet structure and large-sized AgNPs, β -structured coating could induce the formation of pores within the bacterial membrane, which altered the osmotic pressure and then induced membrane collapse. It should be noted that this effect was more inhibitory than lethal. The zeta potential for β group was positive (approximately +21 mV) whereas the zeta potential for m and α groups were negative (approximately -17 mV and -32 mV, respectively). Note that the zeta potential came from both SF micelles and AgNPs/Gen complexes. It meant that the spherical S.aureus were apt to settle on β -structured coating's surface, and undergo severe membrane damage (shown in Fig. 6c). Also, the β structured coating could quickly release a large amount of Ag+, which was also beneficial to its antibacterial ability. Although the release curve showed that the release amount of Ag⁺ in the α structured coating was low, the α -structured coating still exhibited the best anti-adhesion and planktonic bacteria-killing ability, due to its pH-responsive ability and the well-distributed Ag-NPs (20 nm), pH-responsive property significantly improved its antibacterial efficiency, quickly releasing bactericides only when bacterial inflation occurs, a kind of smart response drug-loaded coating. On the other hand, the smaller the particle size of the AgNPs was, the stronger the antibacterial ability was, and it was easier to form a stable complex with Gen, which was beneficial to their synergistic bactericidal effect. However, when it comes to the stability of SF-based coatings, it was closely related to the content of the β sheet structure and was also affected by the physiological environment and adherent bacteria. SEM and Live/Dead staining confirmed that 24 h of exposure to a high concentration of bacterial suspension couldn't cause significant damage and peeling of the SF-based coating, implying acceptable stability of the coating.

In order to verify the long-term antibacterial ability of the SFbased coating, the crystal-violet staining method was used to evaluate the anti-biofilm ability after 7 days of co-cultivation with S. aureus. As shown in Fig. 6f, the surface of the bare Ti was completely covered with a uniform and dense biofilm, which meant that the surface was prone to form a biofilm. Macroscopically, there were many aggregated and large-scale biofilm plaques formed on the surface of the m-structured coating. In comparison, the surface of the α -structured coating was relatively smooth and clean, and there were only a few small areas with scattered purple patches. Quantitative analysis results showed that compared with the bare Ti group, the S.aureus biofilm inhibition rate on the surface of α -structured coating was increased by 85% (Fig. 6e). It should be noted that the α - and β -structured coating had similar ability to inhibit the formation of biofilm, there was no significant difference, and the m-structured coating has the worst ability to inhibit the biofilm development. It should be admitted that the antibacterial rate of α -structured coating didn't exceed 90%, the main reason was that the initial S.aureus concentration was too high $(1 \times 10^8 \text{ CFU/mL})$, and the co-cultivation time reached 7 d, which was much higher than the bacteria concentration in body fluid after implantation surgery, so it could not be said that the coating didn't have the ability to solve orthopedic infection problems. However, the application of the α -structured coating was limited in the case of some serious implant infections or osteomyelitis, but it can be used as a preventive treatment or combined with antibiotic treatment to solve this kind problems. In summary, the results of antibacterial experiments showed that α -structured coating could effectively inhibit bacterial adhesion, planktonic bacteria proliferation and biofilm formation, thereby effectively improving the success rate of implantation surgery.

3.6. Effects of SF-based coatings on cytocompatibility

The most critical determinant of the longstanding implication of an orthopedic implant is depended on the cytocompatibility, in other words, the fate of the regenerating tissue is dictated by the aptitudes of the functional surface to support cellular attachment, proliferation and further expression of fated osteogenic differentiation. Through *in vitro* biocompatible tests, it is possible to have a quick evaluation of the biocompatible property and osteogenic potential of SF-based coatings and estimate their practical application value of. As verified before [47], the thickness of pretreatment PD layer was too thin (<200 nm) and its biological performance was similar with that of pure Ti, sometimes slightly better than pure Ti. Therefore, only pure Ti was chosen as control group to compare with SF-based coatings.

The interaction between the cells and the SF-based coatings' surfaces is a time-dependent process, including cellular attachment, filopodia growth, cytoplasmic webbing, cell cluster formation, and surrounding cytoplasmic changes. Above all, after coculture with MC3T3-E1 for 6 h, the cells on the surfaces of the SF-based coatings were characterized by SEM, Confocal observation, and CCK8-counting, revealing the initial cell adhesion state and proliferation viability. In general, cells can sense the substrate by assembling focal spots and stress fibers, and by stretching the filopodia, and cells tend to change their morphology to adapt to adherent surfaces. Fig. 7a and b showed the adhesion and spreading morphology of MC3T3-E1 cells on the SF-based coatings' surfaces under SEM and Confocal observation, respectively. Obviously, most of the cells attached to the bare Ti had begun to spread, not fully spread, and they were in the initial stage of adhesion. The overall shape was fusiform, and the number of stress fibers and filopodia was small. Quantitative data showed that compared with the bare Ti group, the number of cells on the surface of the α structured coating increased by 18.6%, indicating that the α -helices structure was conducive to cell attachment and proliferation, profiting from hydrophilicity and protein adsorption capacity. In contrast, after 6 h incubation, the number of MC3T3-E1 cells on the surface of the β -structured coating was significantly reduced by 42.7%, and most of the adhered cells were round and aggregated, and the filamentous pseudopods did not appear around the cell, it meant that the high content of β -sheet structure limited the initial adhesion and spreading of the cell to a certain extent, and the surface lacked the contact site for cellular attachment. Another potential possibility was that cells tended to avoid sharp edges of β sheet structures. Also, AgNPs with a diameter larger than 50 nm in the β -structured coating would produce stronger cytotoxicity and interfere with cell adhesion and spreading. In general, the α -structured coating showed better biocompatibility than bare Ti, while the β -structured coating was obviously not conducive to cell adhesion and spreading.

Furthermore, CCK8 assay (measurement of mitochondrial activity) was performed on days 1, 4 and 7 to evaluate the proliferation of MC3T3-E1 cells on SF-based coatings' surfaces. As shown in Fig. 8a, on the first day, the cell proliferation on the surface of the α - and m-structured coatings was slightly lower than that in the bare Ti group, but the cell proliferation showed a time dependence, meaning that the α - and m-structured coatings were not obvious cytotoxicity. After 5 days of co-culture, the number of cells on the surface of the α -structured coating was comparable to that of the bare Ti group, showing accelerated proliferation ability. For the three SF-based coatings, although there was no significant difference in the OD value on the first day (P> 0.05), as the content

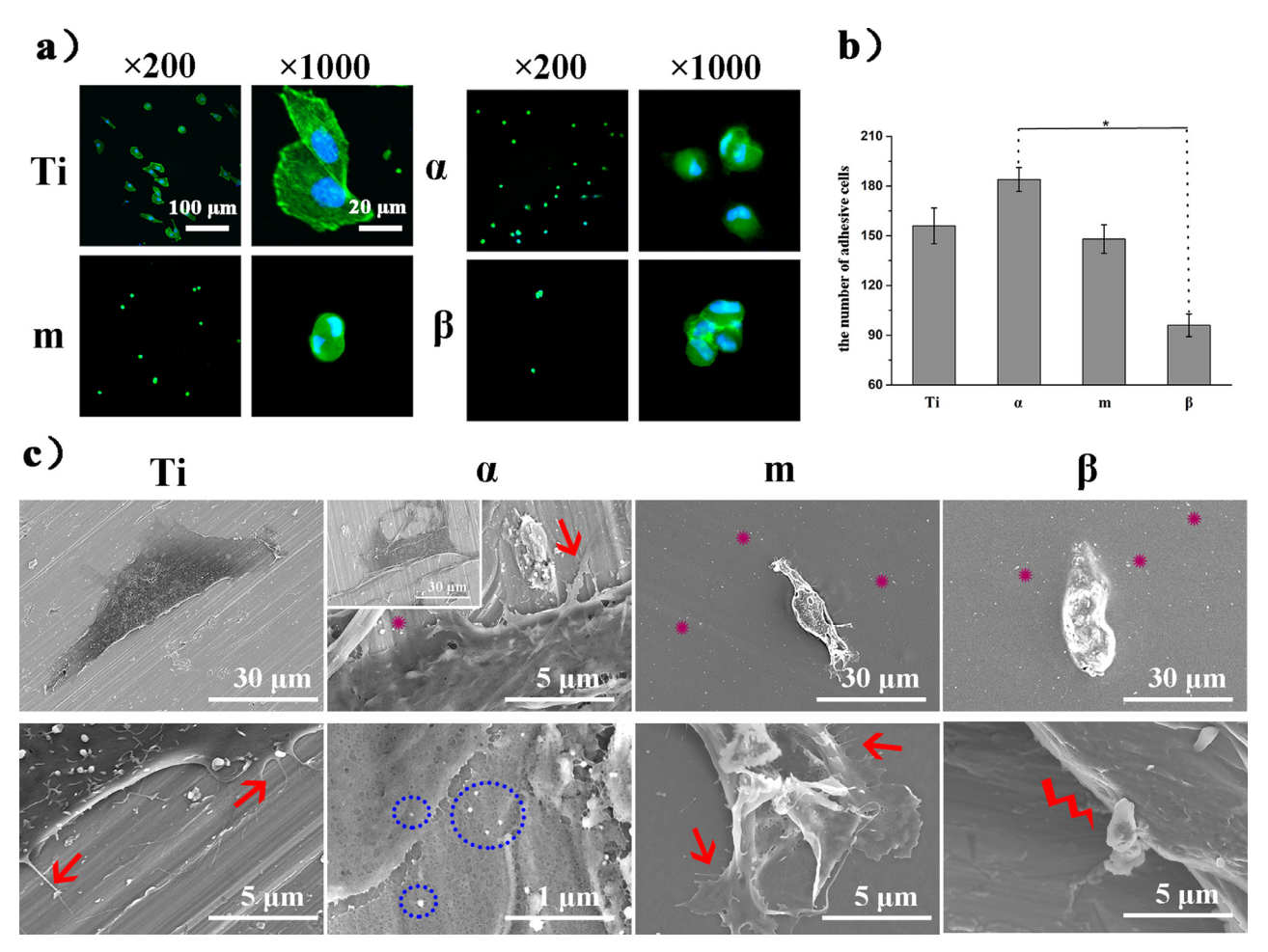


Fig. 7. The cell-coating interfacial interplay during the adhesion-spreading stages: (a) typical fluorescence graphs of nuclei (blue)/F-actin (green) for cells on SF-based coatings; (b) quantification of the nucleus counts; (c) typical attachment and spreading patterns of MC3T3-E1 cells. Arrows indicate pseudopods, and stars indicate AgNPs.(For interpretation of the references to color in this figure legend, the reader is referred to the web version of this article.)

of α -helices structure increased, it was more conducive to the proliferation of MC3T3-E1 cells. The OD value of α -structured coating was significantly higher than that of m- and β -structured coating at 5 days (P <0.05). It can be concluded that α -helices structure was more conducive to cell proliferation than β -sheet structure. However, the influence of AgNPs' particle size and Ag⁺ release behavior on the biological activity of the coating couldn't be ignored. The reduction in particle size was beneficial to reduce the toxicity of AgNPs, and low concentration of Ag⁺ environment would promote cell proliferation. In summary, the α -structured coating benefited from the high content of α -helices structure, small-sized AgNPs and low concentration of Ag⁺ release, which all promoted the adhesion and proliferation of osteoblasts on the surface.

After contact with the SF-based coating, the surface of the cell membrane may trigger a series of toxic cascade reactions as the initial signal of membrane rupture, followed by the outflow of intracellular enzymes (such as lactate dehydrogenase (LDH)), and finally apoptosis, even cell death [48]. In general, once damage to the cell membrane occurs, LDH penetrates into the surrounding medium and exists for a long time in the extracellular environment. Therefore, LDH can be selected as an indicator of the severity of membrane damage and apoptosis. As shown in Fig. 8b, the more LDH produced, the more serious the membrane leakage. It has been verified that the α -structured coating had little effect on the structure of the cell membrane and could be ignored. In comparison, the β -structured coating significantly increased the intracellular stress, leading to apoptosis, but this didn't mean that

the β -structured coating had obvious biological toxicity. A simple fact is that osteoblasts (10-50 µm) are much larger than S.aureus (<1 µm) and tend to respond to external structures. Therefore, bacteria could be influenced by small-sized AgNPs (~10 nm) in the α -structured coating (Fig. 6c), while the cells were hard to sense AgNPs. In contrast, cells were more likely to sense and react to the β -sheet structure, leading to the destruction of cell membrane integrity and leakage of intracellular material (Fig. 8b). Seung Mi Baek et al. [49] have reported that cells on the surface with a higher roughness value and better wettability spread well and developed their fibers widely as a dendritic shape, and the hydrophilic surface (contact angle 30-50°) displayed better adhesion and proliferation of pre-osteoblast cells. From this point of view, the spreading of cells and low LDH expression of α -structured coating were due to two potential reasons: one was that SF had the highest reduction efficiency under the condition of pH 9.5, and more AgNPs (~20 nm) were obtained (Fig. 2), resulting in higher surface roughness; the other reason was that as a natural protein, the higher content of α -helices structure, the better the hydrophilicity of the SF coating, so the α -structured coating owned the best hydrophilic properties and the highest protein adsorption ability (Fig. 4), so the pre-osteoblast cells spread best and formed abundant pseudopods, with the lowest LDH expression and the best cellular integrity.

On the other hand, through certain chemical reactions to verify whether the cells on the surface of the SF-based coating produced excessive intracellular reactive oxygen species (ROS), it was gen-

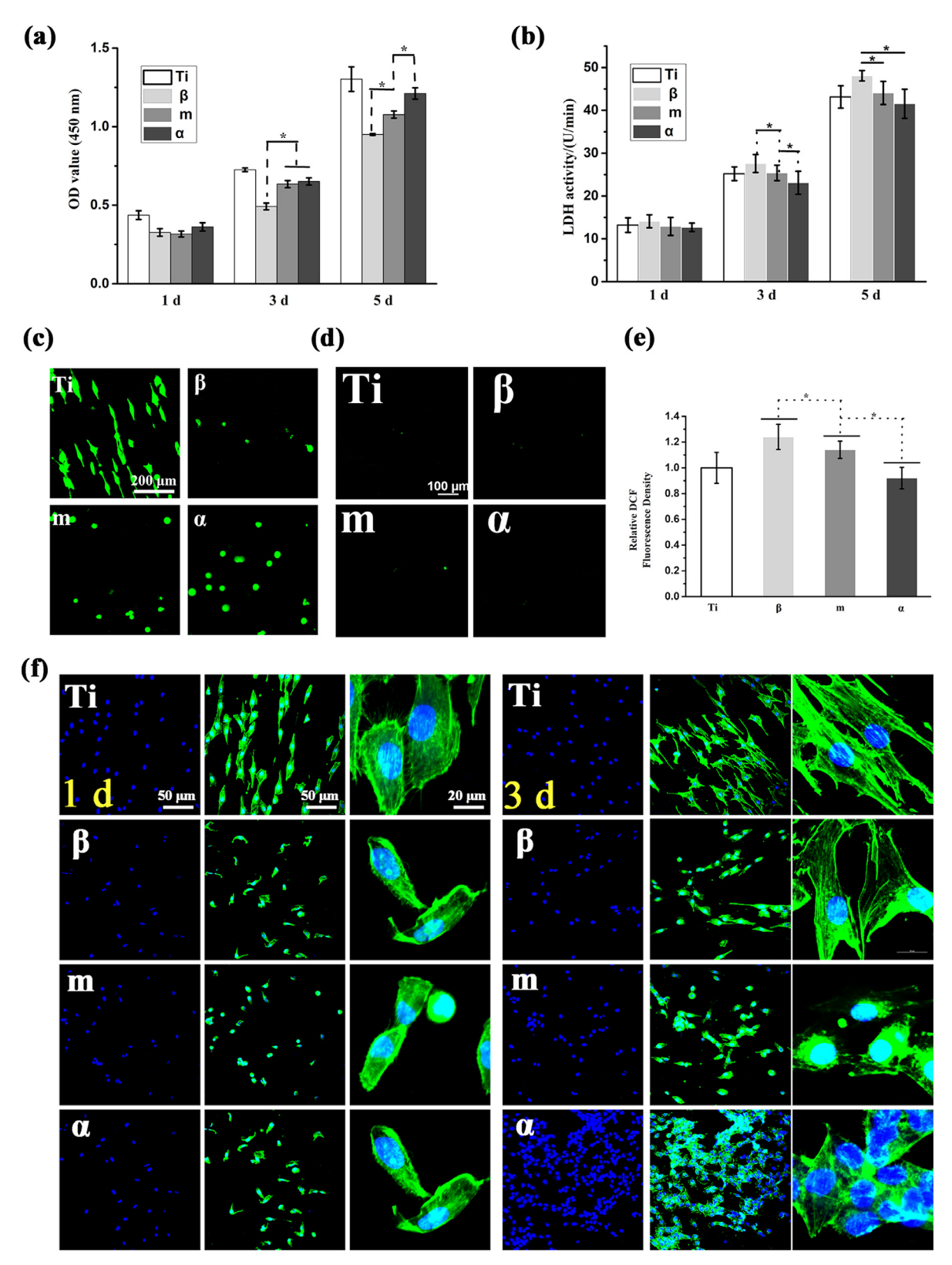


Fig. 8. The cytocompatible and osteoblastic functions of MC3T3 cells: (a) cell viability, and (b) LDH activity at 1-, 3- and 5-d (*p < 0.05); (c) Live/Dead staining of cells for 24 h coculture, green fluorescence indicating cells alive while the red visualizing dead cells; (d,e) Intracellular production of ROS (*p < 0.05); (f) the staining of cytoskeletal actin fibers (green) and nuclei (blue).(For interpretation of the references to color in this figure legend, the reader is referred to the web version of this article.)

erally considered that ROS-induced oxidative stress was the main reason of cytotoxicity [50]. In short, the measurement of intracellular ROS production was to incubate the membrane-permeable DCFH-DA molecules with the cells on the surfaces to generate the highly fluorescent compound DCF through ROS oxidation [51]. Similar to the LDH results, the fluorescence intensity on the surface of the β -structured coating was the highest, which represented the largest amount of intracellular ROS produced, due to the local high concentration Ag⁺ environment generated by the rapid release of the β -structured coating. In comparison, the ROS fluorescence intensity of the surface of the α -structured coating was even lower than that of the bare Ti group, which reflected that the Ag⁺ concentration was low and the attached cells were spreading-well.

However, the high expression of LDH and ROS on the surface of the β -structured coating didn't mean that it would cause apoptosis of the cell, and the surface had no biological activity, because the cell had a certain tolerance to these adverse reactions and could grow through overlapping coverage, which gradually adapted to this situation. This view was validated by cell Death/Live staining after 24 h of co-culture with the sample. As shown in Fig. 8c, there was no obvious dead cells on the surface of the β -structured coating, which meant that high LDH and ROS didn't cause cell apoptosis, but the number of adhered cells was the lowest. In sharp contrast, the number of cells on the surface of the α -structured coating was the largest and the survival state was the best. Then, the cytoskeleton development of MC3T3-E1 cells on the surfaces of SF-based coatings were observed by FITC and DAPI staining, as shown in Fig. 8f. After culturing for 1 day, the cells on the SF-based coatings developed relatively weak stress fibers formed by F-actin, meaning that the SF-based coating inhibited the initial spread of cells to a certain extent. Over the next few days, the stress fibers of the cells on the SF-based coatings continued to assemble, accompanied by proliferation. Even on the surface of the β -structured coating, the cells developed into a network-like fully developed mature cytoskeletal distribution and formed tight connections with surrounding cells. The morphology of MC3T3 cells was further disclosed by SEM observation (Fig. S6). At 3 d, cells on β -structured coating showed the worst spreading state, sparse distribution and some even with a near-round shape. In contrast, most cells on α-structured coating displayed broad-shaped morphologies and eagerly proliferated with numerous elongated lamellipodia overlying surrounded cells, and round cells were hardly noticed.

3.7. Effects on osteogenic differentiation

It is well known that as a typical osteogenic phosphatase, ALP activity level is usually used to assess the initial osteogenic differentiation status of cells. To compare the osteoinductive potential of different SF-based coatings, the ALP levels of cells on the surfaces of the SF-based coatings were tested at day 7 and day 14. As shown in Fig. 9a, the expression of ALP on the surface of the α -structured coating was significantly higher than that of the β structured coating, which was very close to the ALP level of the bare Ti group. With the extension of cultivation time, the expression of ALP in all experimental groups increased significantly, and the amount of ALP expression on the surface of the α -structured coating was 2.5 times that of the β -structured coating, which could be reasonably speculated as the result of the combined effect of AgNPs and β -sheet structure content differences. These results were further confirmed by ALP staining of MC3T3-E1 cells with osteogenic differentiation tendency (Fig. 9b). Osteoblasts with large numbers and dark colors were observed on both the bare Ti and α -structured coating, while the cells on the β -structured coating's surface had the lowest ALP expression, accompanied with few dark and clear cells. Over time, osteoblasts with differential potential continued to secrete collagen, and finally formed an overall bone-like structure through the assembly of collagen fibers and calcium mineralization. Therefore, on the 21st day, we characterized the collagen secretion and mineralization of the cells on the surfaces of the SF-based coatings by SR and ARS staining, respectively. Compared with the β -structured coating, the α -structured coating's surface was larger and darker, showing better collagen secretion from osteoblasts, and the results were even better than the bare Ti group. In addition, the ARS Ca²⁺ content was measured on the 28th day (Fig. 9c), which was consistent with the collagen staining results. Unsurprisingly, the largest and clearest calcium nodules were observed on the surface of the α -structured coating, indicating the strong ability of coating to electrostatically combining with Ca²⁺. The formation rate of the compound Ca-P played a key role in the osteoblast mineralization process, which mainly depended on the number of electrostatic adsorptions of Ca²⁺ and PO₄³⁻ ion functional groups on the surface of the SF-based coating. Due to the presence of more hydrophilic groups on the surface of the α -structured coating, in liquid environments, the α -helices structure tended to adsorb mineral ions and formed mineralized nodules.

3.8. Osteo-related genes expression

The tests on the expression of a series of osteogenic genes in cells revealed the interaction of SF-based coatings with osteoblasts, and the initialization and completion of various cell functions, which were closely related to the osteogenic differentiation. After 7 and 14 days of co-culture, the expression of genes related to osteogenesis (OCN, Col1a1, Runx2, etc.) in MC3T3-E1 cells on the surface of SF-based coatings was analyzed by Q-PCR experiment. Compared with the bare Ti group, genes related to osteogenesis (including ALP, OCN, Col1a1, and Runx2) of cells on the surface of the α -structured coating were significantly up-regulated (Fig. 9hk), along with the highest expression levels, indicating low β -sheet contents and the small size of AgNPs, which were conducive to the osteogenic differentiation of cells. Specifically, after the cells were cultured on the surface of the α -structured coating for 7 and 14 days, the expression of Runx2 was 2.7 times and 1.9 times that of the bare Ti group (Fig. 9h). In fact, Runx2 could significantly regulate the initial bone formation and the function of osteoblasts after differentiation, which played a vital role in stimulating osteoblast differentiation, inhibiting chondrocyte and adipocyte differentiation and up-regulating the expression of bone matrix genes (OCN, Col1a1, etc.) [52]. Similarly, when MC3T3-E1 cells were incubated on the surface of the α -structured coating for 14 days, OCN gene expression was the highest, which was 3.3 times that of the bare Ti group (Fig. 9i). Generally, the high level of OCN expressed by differentiated cells was closely related to the mineralization process of osteoblasts, and the highest expression was reached during the mineralization process [53]. In contrast, cells on β -structured coating had the lowest OCN expression, which was consistent with the previous calcium deposition staining results, which meant that the mineralization process of osteoblasts was inhibited. Even though there was no significant difference in the expression of Col1a1 in each group on Day 7, the expression of Col1a1 of cells on the surface α -structured coating on Day 14 was significantly higher than that in other groups (Fig. 9g). Col1a1 was a protein related to the bone formation, existing in the extracellular bone matrix, and affecting the cell's osteogenic behavior [54]. In addition, the typical bone differentiation marker ALP was most expressed on the surface of the α -structure coating after 7 and 14 days. In summary, the content of β -sheet structure and the size of AgNPs of the SFbased coatings affected the expression of osteoblast-related genes, thereby affecting the bone differentiation ability of cells.

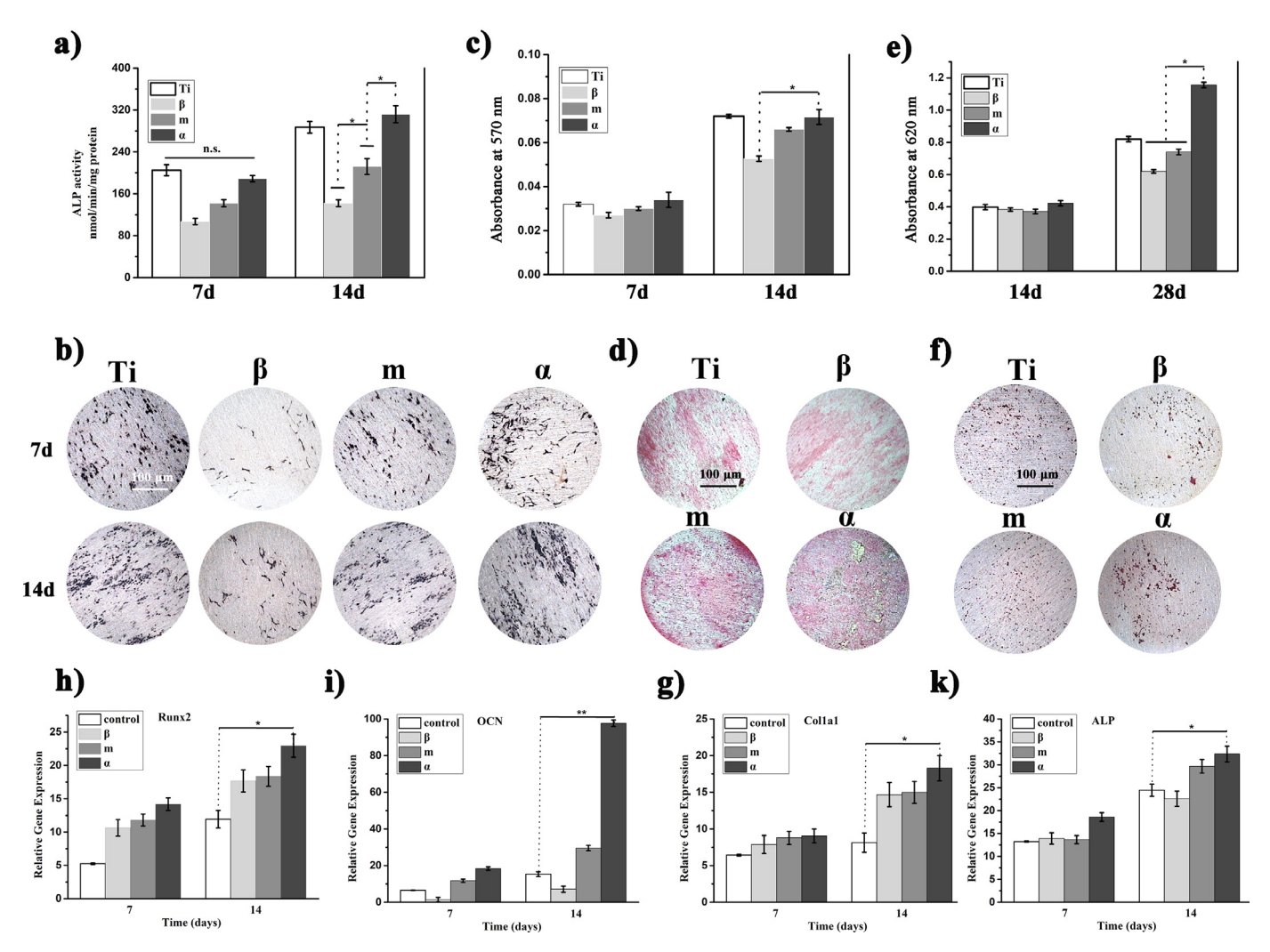


Fig. 9. Osteogenic activates of MC3T3 cultured on samples. (a) ALP activity; (b) ALP positive areas of MC3T3 cultured for 7 days; quantification of collagen secretion (c) and calcium deposition (e); coloration of the collagen (COL) secretion (d, purplish red) and calcium (CAL) deposition (f, red or purplish red) on different specimens for 28 days; (h-k) Q-PCR analysis for osteo-related genes including OCN, Col1a1, Runx2, and ALP: the effect of different matrixes on osteo-related gene expression (For interpretation of the references to color in this figure legend, the reader is referred to the web version of this article.).

3.9. in vivo results

3.9.1. Subcutaneous tissue compatibility in vivo

According to the results of antibacterial and biocompatibility in vitro, Ti-based implant with modified surface of α -structured coating was selected for in vivo experimental study, and bare Ti was used as a control group. The histocompatibility of the lphastructured coating was characterized by histological sections 30 days after implantation under rabbit skin [55]. As shown in Fig. 10, the two groups of implants were obviously wrapped with new tissue, and no representative foreign body reaction was found. For the experimental group, even if a small amount of spindle-forming fibroblasts (red star) were observed, no phagocytic cells and inflammatory reactions were observed in the surrounding conjunctival tissues, meaning that the local diffusion of Ag+ released from the α -structured coating did not cause any immunity reaction and biological toxicity. In addition, the quantitative calculation results of the number of fibroblasts and the thickness of the capsule were used to characterize the difference in tissue response between α structured coating and bare Ti. As shown in Fig. 10b, the number of fibroblasts on the α -structured coating was close to that of bare Ti, and the average thickness of the capsule (382.6 \pm 20.7 mm)

was almost twice that of the bare Ti group (197.3 \pm 23.5 mm), which indicated that the α -structured coating obviously improved the biocompatibility of the implant and promoted the growth of fibrous membranes. All in all, the results of subcutaneous implantation showed that the α -structured coating did not cause allergic reactions and other rejection reactions in the body, which was similar to or even lower than the toxicity of the bare Ti group. According to the release curve of Ag⁺ (Fig. 5d), the α -structured coating showed a clear slow-release curve under physiological conditions. Only about 35% of Ag+ was released outside the body within 24 h immersion, and the subsequent release rate of Ag⁺ remained at very low levels, the results of subcutaneous implantation indicated that Ag+ released into the local environment did not induce toxic reactions. Compared with bare Ti, implant modified with α structured coating caused some foreign body reaction in the early stage, but over time, this harmful effect was gradually weakened (low concentration release of Ag+ after 24 h). In addition, it could not be ignored that the flowing body fluid diluted the concentration of Ag+, which effectively reduced the acute inflammatory reaction [56]. It can be concluded that low concentrations of Ag+ would not only produce biotoxicity, but even promote the integration of the implant and surrounding encapsulated tissue. In ad-

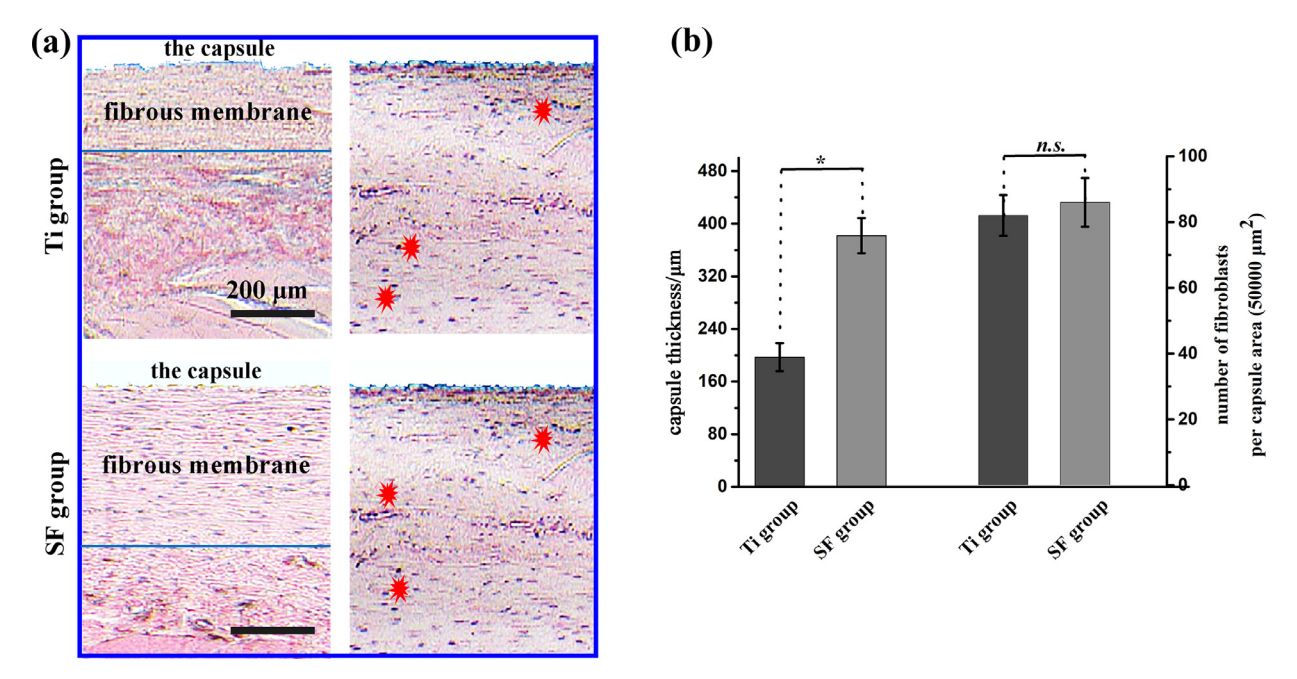


Fig. 10. *In vivo* biocompatibility: (a) representative H-E stained images of soft tissues formed on the samples' surfaces following 30-d subcutaneous implantation; (b) results of the histological analysis of capsule thickness and fibroblast number.

dition, studies have confirmed that SF-based biomaterials will not cause hypersensitivity reactions or other foreign body reactions in rats [57]. Ten days after implantation of SF fibers in mice, inflammation of neutrophils subsided significantly, and SF fibers gradually fused in cell-rich connective tissues and initial blood vessel formation occurred [58]. The above results indicated that the SF-based coating didn't cause an immune response and had biological activity.

3.9.2. Micro-CT analysis

The ideal and feasible drug-loading coating can be applied not only to two-dimensional surfaces, but also to unique and complex implants, because currently popular implants with big potential value are usually built into complex geometric shapes (e.g. dental implants, hip and knee prostheses). In view of this, the functional coating used for surface modification should have an appropriate degree of flexibility to adapt to implants with complex structures to meet individual needs. Recently, the 3D printed porous Ti6Al4V scaffold has shown great promise in the field of orthopedic implantation. It was satisfactory that α -structured coating (wet chemical treatment) could be used for the surface-modified porous Ti6Al4V scaffold. Therefore, the rabbit femoral defect model was used to verify the *in vivo* osseointegration ability of the porous Ti6Al4V scaffold modified with α -structured coating.

In order to study the osseointegration ability of the porous Ti6Al4V scaffold modified with α -structured coating, the implants were implanted in rabbit femur for 8 weeks to study the bone remodeling [59]. As shown in Fig. 11a, where the new bones were marked in green, the scaffold modified with α -structured coating was completely covered with new bone, while the bare scaffold contained a lot of pores, together with less amount of new bone. Compared with bare scaffolds, α -structured coating could promote more new bone formation in the area of implant/tissue interface, which meant that the implant and new bone were well fused. In addition, the bone volume/total tissue volume ratio (BV/TV) was analyzed based on Micro-CT data to quantify the formation of new bone. The BV/TV fraction of the experimental group was 41.8 \pm 4.0%, and that of the bare scaffold was 29.0 \pm 3.7% (Fig. 11b). As shown in Fig. 11c, the scaffold, the new bone in

the implant, and the holes in the scaffold were marked as black, green, and yellow, respectively. It could be clearly observed in the top view and the side view that the scaffold modified by the α -structured coating had more pronounced new bone formation. Based on these results, for the porous Ti6Al4V scaffold, the α -structured coating not only enhanced the growth of new bone on the coating surface, but also enhanced the bone ingrowth.

3.9.3. Quantitative and qualitative histological results

As shown in Fig. 12a, the bare scaffold and the scaffold modified with α -structured coating were implanted into the rabbit femur, and the typical histological image of the cross section was stained. The red area represented the mineralized trabecular bone and the black indicated a porous support. For bare scaffold, the ingrowth bone was loosely in contact with the edge of the implant, there was no effective integration, and only partially mineralized new bone was produced in the surrounding area. In contrast, the porous scaffold modified with α -structured coating showed a highly mature new bone-implant fusion. The regenerated new bone fused almost all the edges of the implant, and a large number of new bones were growing (Fig. 12a). As shown in the enlarged view, the new bone was not only fused with the boundary of the α -structured coating modified porous scaffold, but also connected to the adjacent new bone through a "bridge", which meant that it has better osteoinductivity and implant stability. Fig. 12b and c were the quantitative calculation results of BI and BICR, respectively. The BI and BICR of porous scaffold modified by α -structured coating were much higher than bare scaffold, which meant that the functional coating significantly improves the osseointegration ability of the scaffold surface.

Compared with bare scaffold, the percentage of contact between the α -structured coating modified scaffold and the new bone increased by 138.3% (35.15 \pm 2.9% vs 14.75 \pm 3.5%, p <0.05), and the BI of the α -structured coating modified scaffold was also increased, up to 280.1% (78.3 \pm 3.2% vs 20.6 \pm 2.4%, p <0.05). In addition, we also noticed the poor bone growth of the bare scaffold, which was contrary to previous reports. It was reported that a large number of new bones would be generated in and around the Ti alloy scaffold implanted in the animal. For exam-

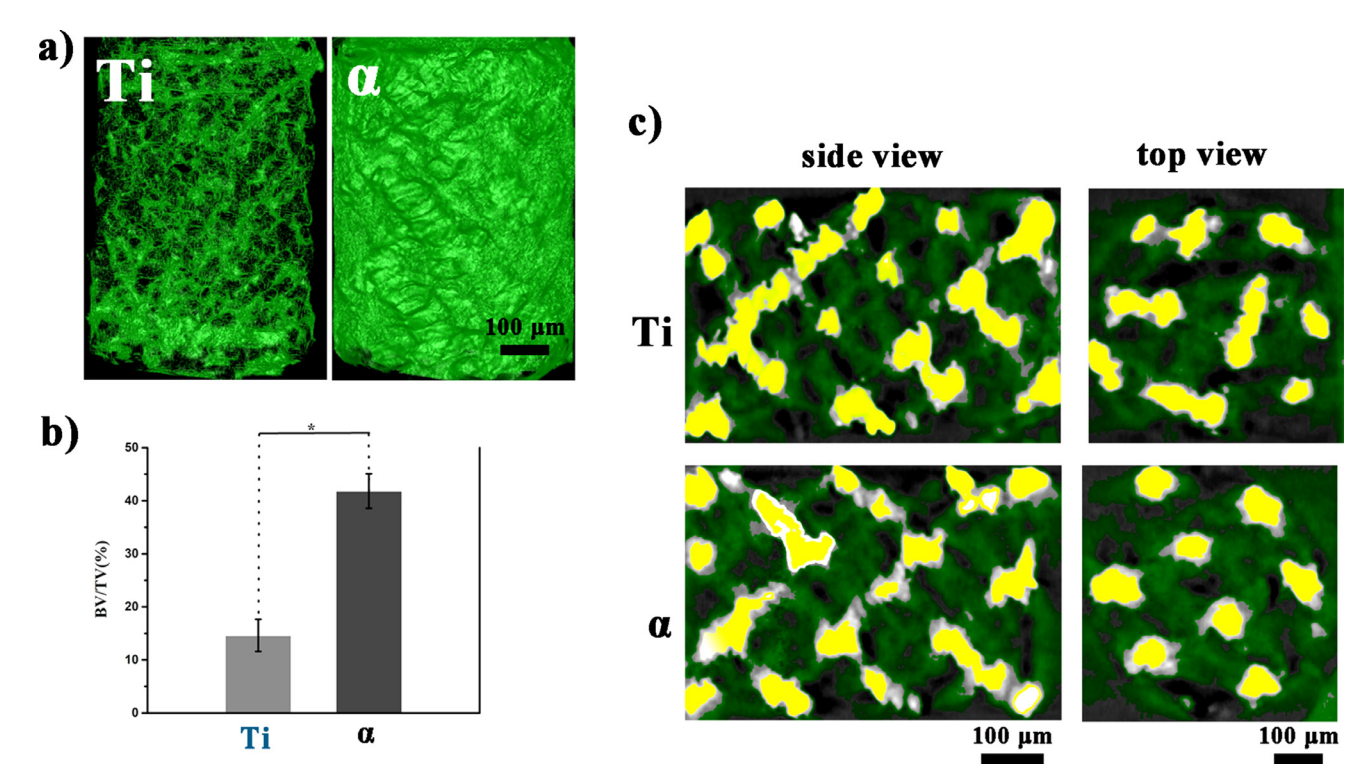


Fig. 11. Micro-CT images of the untreated and SF coating treated porous Ti6Al4V scaffolds after 8 weeks of *in vivo* implantation. (a) 3D reconstruction of the scaffolds: new born bone was labeled with bright green; (b) the quantitative results of bone volume/total tissue volume (BV/TV); (c) Micro-CT images: the implants, pores and bones within the scaffold are labeled black, yellow and deep green, respectively. *Significant difference. Sample number in each group is 4. (For interpretation of the references to color in this figure legend, the reader is referred to the web version of this article.)

ple, Ponader et al. [60] reported that the BI value of the Ti-based scaffold implanted in the frontal bone of pigs was relatively high, 30% and 46% at 30 and 60 days, respectively. However, Takemoto et al. [61] observed that the growth of new bones on bare Ti alloy scaffold in the rabbit model was very weak (BI: 9.8 \pm 4.2%), even worse than our results. We reasonably speculated that the new bone formation in rabbits was relatively poor compared to other larger animal models due to the lack of inherent trabecular bone. For example, Lopez-Heredia et al. [62] reported that in a similar rabbit model, the bone growth of the bare scaffold was time-dependent: a large amount of new bone formation was observed at week 3, and due to the inherent bone remodeling, only an ingrown bone was detected on the periphery of the scaffold. This part explained that the reason for the poor bone integration of the bare scaffold in the study was excessive bone remodeling. Undoubtedly, the choice of animal model and the effect of bone remodeling on the results should be considered, resulting in a difference between the α -structured modified scaffold and the bare scaffold in terms of new bone formation inside the scaffold.

As shown in Fig. 12d, the fluorescent-labeled microphotographs revealed different bone growth patterns between the α -structured coating modified scaffold and the bare scaffold. Obviously, the entire edge of the α -structured coating modified scaffold was surrounded by strong green fluorescence, which meant that new bones were formed and mature, and the scaffold and the new bone were rapidly fused (Fig. 12d). However, only part of the edge of the bare scaffold was covered with relatively dark fluorescent staining, and the amount of new bone was low. As shown in the enlarged image (Fig. S7), not only the initial bone formation (marked in green) that occurred in the outer surface and the inner pores at the interface of the α -structured coating modified scaffold, but also a strong signal of bone expansion to the outer space (orange). During the entire osseointegration process, the formation of new bones

clearly appeared on the surface of the α -structure coating modified scaffold, which was a contact osteogenesis mode [61]. For the control group, the formation and expansion of new bones (green and orange) were hardly marked by fluorescent markers. The early stage of osseointegration showed that new bones were mainly generated near the host bone and then developed toward the implant surface, an indirect way of growth.

3.10. The mechanism of antibacterial and osteoinductive property

In order to further reveal the influence of the β -sheet structure content and AgNPs' size of the SF-based coating on its antibacterial and osteointegration ability, a series of different AgNPs/Genloaded SF-based coatings were constructed by adjusting the forming pH and temperature. All in all, the optimized α -structured coating showed pH-responsive antibacterial properties, biocompatibility, and the ability to promote osteogenesis in vivo. From an antibacterial point of view, the α -structured coating displayed anti-adhesion, planktonic bacteria-killing, and biofilm formation inhibition capabilities. Its antibacterial mechanism was mainly pH-responsive bacteria-killing, which was an intelligent response type functional coating, while the β -structure coating mainly relied on structural bacteria-killing. Specifically, due to the high content of α -helices structure in the α -structured coating and the small size of AgNPs (about 10 nm), there was a distinctive pHdependent Ag+ release behavior, that was, long-term sustained release under physiological conditions, and the accelerated release of antibacterial agents triggered by acidic conditions, therefore, the α -structured coating exhibited high-efficiency antibacterial properties. As shown in Fig. 5d, after immersed in neutral PBS solution (pH 7) for 24 h, the m and β -structured coating released 56.2% and 72.5% of Ag+, compared with only 35.4% of the α -structured coating (\sim 370 µg). In contrast, the α -structured coating released

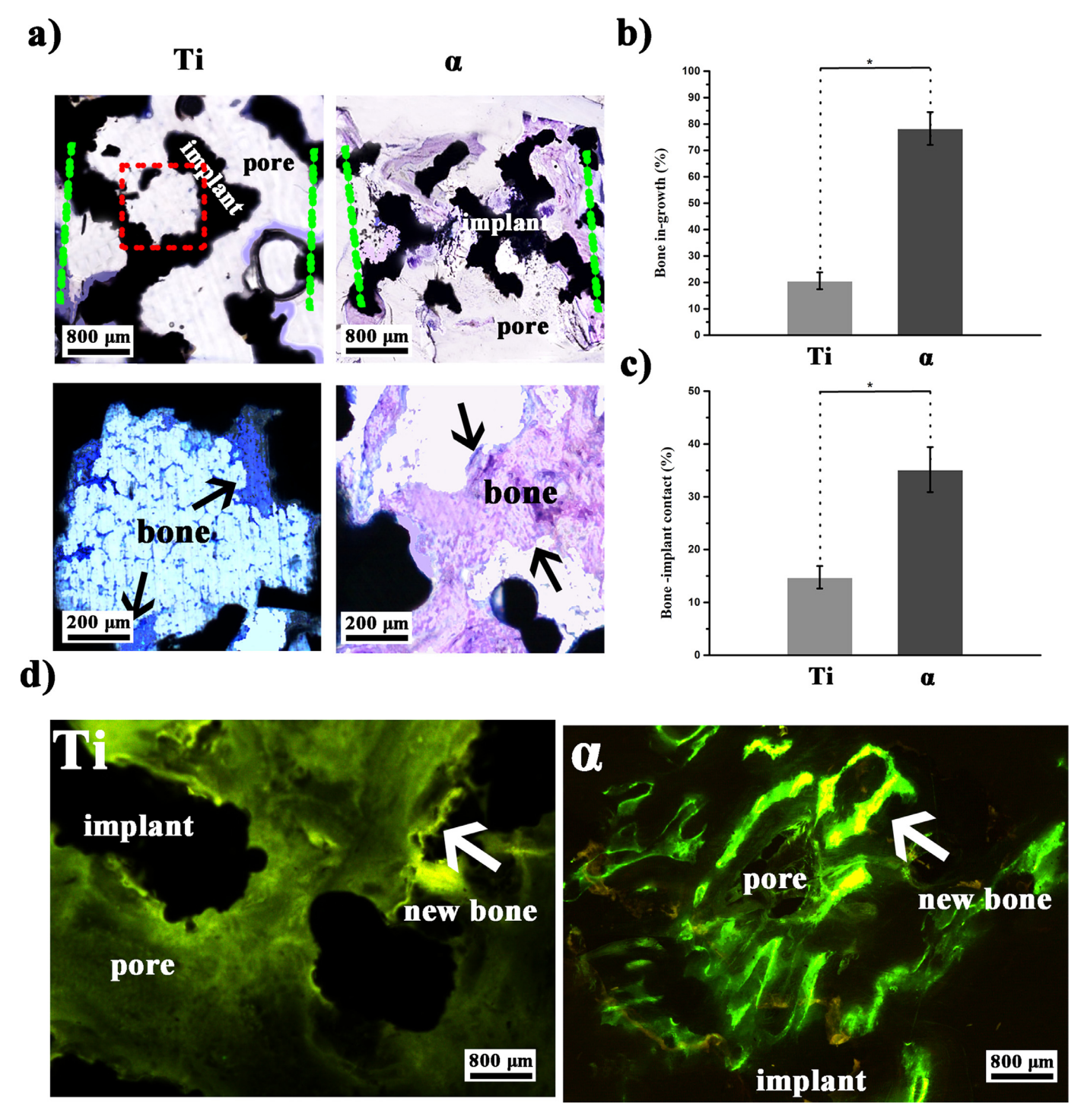


Fig. 12. (a) Histological sections and the magnified images at the selected area of the untreated scaffold and SF coating-decorated scaffold. Green dotted line ("-") indicates the scaffold/tissue margin; (b, c) Quantitative results of bone in-growth and bone-implant contact ratio of the 2 types of implants; *p < 0.05. Sample number in each group is 8; (d) The fluorescent images of the SF coating-treated and untreated scaffold, respectively. Red dotted line ("-") indicates the scaffold/tissue margin. The bone-formation fronts at the 3rd and 7th week are marked by a green label from calcein green and an orange label from tetracycline, respectively. (For interpretation of the references to color in this figure legend, the reader is referred to the web version of this article.)

62.7% of Ag $^+$ (~680 µg) when immersed in an acidic PBS solution (pH 4) for 24 h, which was about twice that of the neutral solution. The above all showed that the α -structured coating had a pH-responsive and the initial burst release suppressed performances, which were beneficial to its long-term antibacterial ability. It has been confirmed that the smaller the particle size of AgNPs, the stronger its biological toxicity, which was also conducive to the improvement of the antibacterial properties of the α -structured coat-

ing. At the same time, the small-size, uniformly distributed AgNPs was more likely to complex with the Gen molecule and exerted a synergistic bactericidal effect [12]. On the other hand, as shown in Fig. 5, the pH-dependent bactericides release behavior gave α -structure coating a property of bacteria-triggered killing, long-term retention of bactericides 'antibacterial activity in the coating, only when the bacteria adhered to the coating surface, the secreted acid mucopolysaccharide caused local acidification, causing the coat-

ing to release antibacterial agents for bacteria killing. When it comes to β -structure coating, the burst release of Ag+ was the main source of its antibacterial ability, another possible reason was the physical damage of bacteria caused by the high content of β -sheets structure as nanoneedle. It should be pointed out that after coculture with S.aurues (1 \times 10 8 CFU/mL) for 7 d, the α - and β -structured coating displayed similar ability to inhibit the formation of biofilm. However, antibacterial agent release performance of β -structured coating had the problem of initial burst release, and the later low concentration release was easy to cause bacterial resistance.

As we all know, osteoblasts need to adhere to a suitable coating surface to survive, and cell-coating interactions play a vital role in the cellular functionalization, such as spreading, proliferation, and differentiation [63]. Therefore, the interaction between osteoblasts and SF-based coatings was systematically studied in detail. Cell adhesion was mainly mediated by a series of membrane proteins (called integrins). In addition, cells could also adhere to the coating through some certain non-specific interactions, which were mainly affected by the hydrophilicity and hydrophobicity of the coating surface [64]. According to the contact angle and protein adsorption results, the α -structured coating showed better hydrophilicity and protein adsorption capacity, which meant that the α -structured coating was beneficial to the cell-coating interaction. Nevertheless, compared with the bare Ti group, the cells on the surfaces of the SF-based coatings presented poor adhesion and spreading in the early stage (less than 24 h). Studies have shown that after 12 h of inoculation, the number of human mesenchymal stem cells adhering to the SF scaffold is significantly lower than PGA (17 \pm 2% vs35 \pm 4%) [65]. Also, researches showed that both endothelial and fibroblastic cells presented weak attachment on SF matrixes, which was closely related to its second structure contents and forming conditions [66]. However, with the extension of the culture time (more than 3 days), this adverse effect was often negligible, especially for the α -structured coating, which displayed the best cell spreading and proliferation status. Especially in the study of promoting osteogenic differentiation, α -structured coating significantly increased the expression of ALP, ECM secretion and calcium deposition of osteoblasts (Fig. 9). As shown in Fig. 13, we speculated that the biocompatibility of the α -structured coating and the mechanism of promoting bone formation were as follows: (1) the α -structured coating showed relatively high hydrophilicity and protein adsorption capacity, which was beneficial to cells adhesion and further osteogenesis differentiation; (2) the high content of α -helices structure was conducive to cell adhesion, proliferation and expression of certain osteogenic signals; (3) due to the pH-dependent release of Ag+, the low concentration of Ag⁺ local environment was conducive to cell proliferation and osteogenic differentiation [67].

The immune response related to SF has been widely studied. SF can inhibit the secretion of certain inflammatory signals (such as IL-1 β and cyclooxygenase 2), resulting in extremely low immune response levels [65,68,69]. As shown in Fig. 10, no immune response was observed after the subcutaneous implantation of the Ti implant modified with α -structure coating, which also promoted the growth of the capsule. The results of rabbit femur implantation confirmed that the porous Ti6Al4V scaffold modified with α structured coating showed close contact between the new bone and the scaffold, while the bare scaffold showed an indirect new bone growth pattern. In comparison, the high content of α -helices structure and the small size AgNPs were conducive to promoting the formation of new bone and the enhancement of the bond between bone and scaffold. Through micro-CT images, new bones were formed at most of the outer edge and inner hole of the scaffold modified with α -structured coating, indicating that the early fixation effect of α -structured coating (Fig. 11). This result was consistent with previous studies. After 8 weeks of critical size rat skull implantation, the SF membrane (8.75 \pm 0.80 mm) showed an absolute volume of new bone formation similar to the commercial collagen membrane (8.47 \pm 0.75 mm). In addition, 3 weeks after implantation in the rabbit femur model, no bone remodeling of ingrowth bone was observed, which means that the α -structured coating may inhibit the bone remodeling process. According to the histological staining results, the porous scaffold modified by the α structured coating showed enhanced new bone ingrowth. It was speculated that its growth mechanism was as follows: early neonatal bone (green fluorescence) was widely formed at the edge of the scaffold, and also acts as a bridge between the edge of the implant and the autogenous bone induces the implant and bone to fuse together. Shahram et al. [70] have demonstrated that formic acid-treated SF scaffold can begin to integrate into the surrounding tissues 3 days after implantation, and obvious vascularization occurs between 15 and 180 days, and the scaffold continued to degrade during the first 90 days [71]. It is worth noting that there are recent reports that both SF and Ag directly affect the signaling pathways related to osteogenesis. For example, SF can inhibit the expression of Notch signal and induce the enhanced expression of ALP and Runx2 mRNA [72]. In addition, it has been reported that SF scaffolds accelerate bone repair through WNT signaling, which involves regulating cell activity (migration, proliferation, differentiation, cell death) and determining the process of bone integration [73]. On the other hand, Hui et al. reported that AgNPs can activate RhoA signaling, leading to actin polymerization, and then induce the expression of osteogenic signals in human bone marrow

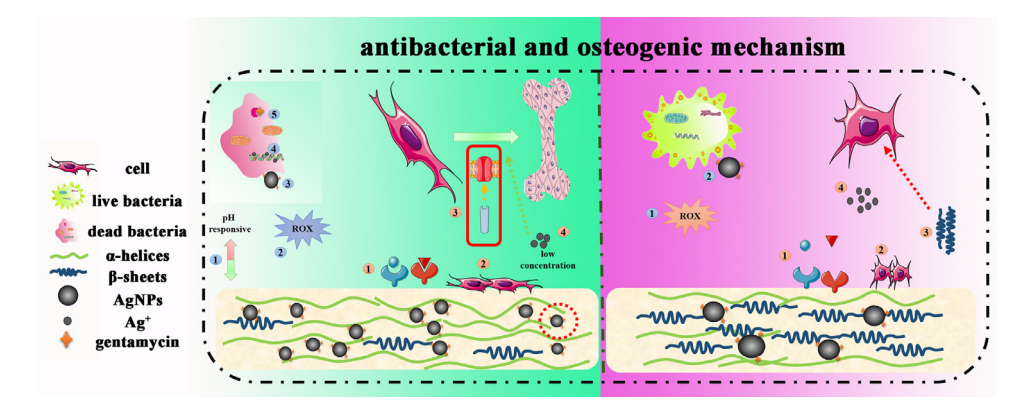


Fig. 13. Schematic illustration of the potential antibacterial and osteogenic mechanism of α coating (left green part) and β coating (right pink part). The antibacterial paths of α coating: (1) bacteria induced release of Ag⁺; (2) ROS generation; (3) bacterial membrane damage; (4) DNA and protein synthesis damage. The osteogenic paths of α coating: (1) adsorption of protein and growth factors; (2) cell attachment and proliferation; (3) intervening several osteogenic gene pathway; (4) low concentration Ag⁺ promoted osteogenic differentiation.(For interpretation of the references to color in this figure legend, the reader is referred to the web version of this article.)

stem cells [67]. Based on the above analysis, the porous scaffold modified with α -structured coating owned potential to enhance osseointegration *in vivo*, and achieve the purpose of osseointegration by promoting the formation of new bone and inhibiting bone remodeling and resorption.

4. Conclusion

In this paper, by controlling the parameters of pH and temperature, AgNPs/Gen-loaded SF coatings with varying structure and components were successfully constructed on the Ti surface to improve antibacterial and osteogenic abilities. Among these coatings, α coating contained the lowest content of β -sheets content (19.0%) and the smallest AgNPs (~20 nm). This hydrophilic coating tended to adsorb protein and released Ag+with a pH-dependent, accelerated release at acidic condition. Benefiting from pH-dependent release behavior of AgNPs, α coating could effectively inhibit bacterial attachment and biofilm formation. Even with a relatively weak spreading state at initial stage, preosteoblast MC3T3-E1 cells were apt to attach on the surface and showed an improved proliferation for a long period. In vitro osteogenic tests, cells anchoring on α coating showed high ALP expression, collagen secretion and calcium mineralization, implying a strong osteogenic differentiation potential. Through subcutaneous and rabbit femoral defect model implantation, the resultant coating elicited no inflammatory response, and strongly improve the new-bone generation, strong interaction of implant-bone. Taken together, the optimized α coating should be helpful for the construction of bioactive surface with superiorly antibacterial and osteogenic properties, highly improving the success rate of orthopedic implant surgery.

Data availability statement

All data generated or analyzed during this study are included in this article or supplementary information files. The raw/processed data required to reproduce these findings cannot be shared at this time as the data is also from part of an ongoing study.

Declaration of Competing Interest

The authors declare that they have no known competing financial interests or personal relationships that could have appeared to influence the work reported in this paper.

The authors declare the following financial interests/personal relationships which may be considered as potential competing interests:

Acknowledgment

This work is jointly supported by the National Key R&D Program of China (2018YFC1106600) and National Natural Science Foundation of China (No. 31670974, No. 31370954).

Supplementary materials

Supplementary material associated with this article can be found, in the online version, at doi:10.1016/j.actbio.2020.08.040.

References

- [1] G.-J.A. ter Boo, D.W. Grijpma, T.F. Moriarty, R.G. Richards, D. Eglin, Antimicrobial delivery systems for local infection prophylaxis in orthopedic-and trauma surgery, Biomaterials 52 (2015) 113–125.
- [2] O. Rzhepishevska, N. Limanska, M. Galkin, A. Lacoma, M. Lundquist, D. Sokol, S. Hakobyan, A. Sjöstedt, C. Prat, M. Ramstedt, Characterization of clinically relevant model bacterial strains of Pseudomonas aeruginosa for anti-biofilm testing of materials, Acta Biomater. 76 (2018) 99–107.

- [3] J. Min, K.Y. Choi, E.C. Dreaden, R.F. Padera, R.D. Braatz, M. Spector, P.T. Hammond, Designer dual therapy nanolayered implant coatings eradicate biofilms and accelerate bone tissue repair, ACS Nano 10 (2016) 4441–4450.
- [4] J.R. Morones-Ramirez, J.A. Winkler, C.S. Spina, J.J. Collins, Silver enhances antibiotic activity against gram-negative bacteria, Sci. Transl. Med. 5 (2013) 190r.
- [5] W. Zhou, Z. Jia, P. Xiong, J. Yan, Y. Li, M. Li, Y. Cheng, Y. Zheng, Bioinspired and biomimetic AgNPs/gentamicin-embedded silk fibroin coatings for robust antibacterial and osteogenetic applications, ACS Appl. Mater. Interfaces 9 (2017) 25830–25846.
- [6] H. Chouirfa, H. Bouloussa, V. Migonney, C. Falentin-Daudré, Review of titanium surface modification techniques and coatings for antibacterial applications, Acta Biomater. 83 (2019) 37–54.
- [7] L. Rizzello, P.P. Pompa, Nanosilver-based antibacterial drugs and devices: mechanisms, methodological drawbacks, and guidelines, Chem. Soc. Rev. 43 (2014) 1501–1518.
- [8] J.-C. Jin, Z.-Q. Xu, P. Dong, L. Lai, J.-Y. Lan, F.-L. Jiang, Y. Liu, One-step synthesis of silver nanoparticles using carbon dots as reducing and stabilizing agents and their antibacterial mechanisms, Carbon N Y 94 (2015) 129–141.
- and their antibacterial mechanisms, Carbon N Y 94 (2015) 129–141.
 [9] I. Zhuk, F. Jariwala, A.B. Attygalle, Y. Wu, M.R. Libera, S.A. Sukhishvili, Self-defensive layer-by-layer films with bacteria-triggered antibiotic release, ACS Nano 8 (2014) 7733–7745.
- [10] J. Melke, S. Midha, S. Ghosh, K. Ito, S. Hofmann, Silk fibroin as biomaterial for bone tissue engineering, Acta Biomater. 31 (2016) 1–16.
- [11] W. Zhang, L. Chen, J. Chen, L. Wang, X. Gui, J. Ran, G. Xu, H. Zhao, M. Zeng, J. Ji, Silk fibroin biomaterial shows safe and effective wound healing in animal models and a randomized controlled clinical trial, Adv. Healthc. Mater. 6 (2017) 1700121.
- [12] W. Zhou, Z. Jia, P. Xiong, J. Yan, Y. Li, M. Li, Y. Cheng, Y. Zheng, Bioinspired and biomimetic AgNPs/gentamicin-embedded silk fibroin coatings for robust antibacterial and osteogenetic applications, ACS Appl. Mater. Interfaces 9 (2017) 166–173.
- [13] J. Yan, W. Zhou, Z. Jia, P. Xiong, Y. Li, P. Wang, Q. Li, Y. Cheng, Y. Zheng, Endowing polyetheretherketone with synergistic bactericidal effects and improved osteogenic ability, Acta Biomater. 79 (2018) 216–229.
- [14] W. Zhou, Y. Li, J. Yan, P. Xiong, Q. Li, Y. Cheng, Y. Zheng, Construction of self-defensive antibacterial and osteogenic AgNPs/gentamicin coatings with chitosan as nanovalves for controlled release, Sci. Rep. 8 (2018) 13432.
- [15] X. Fei, M. Jia, X. Du, Y. Yang, R. Zhang, Z. Shao, X. Zhao, X. Chen, Green synthesis of silk fibroin-silver nanoparticle composites with effective antibacterial and biofilm-disrupting properties, Biomacromolecules 14 (2013) 4483– 4488
- [16] X. Shen, Y. Zhang, Y. Gu, Y. Xu, Y. Liu, B. Li, L. Chen, Sequential and sustained release of SDF-1 and BMP-2 from silk fibroin-nanohydroxyapatite scaffold for the enhancement of bone regeneration, Biomaterials 106 (2016) 205–216.
- [17] M.B. Applegate, B.P. Partlow, J. Coburn, B. Marelli, C. Pirie, R. Pineda, D.L. Kaplan, F.G. Omenetto, Photocrosslinking of silk fibroin using riboflavin for ocular prostheses, Adv. Mater. 28 (2016) 2417–2420.
- [18] L. Li, S. Puhl, L. Meinel, O. Germershaus, Silk fibroin layer-by-layer microcapsules for localized gene delivery, Biomaterials 35 (2014) 7929–7939.
- [19] K. Cai, Y. Hu, K.D. Jandt, Surface engineering of titanium thin films with silk fibroin via layer-by-layer technique and its effects on osteoblast growth behavior, J. Biomed. Mater. Res. Part A 82 (2007) 927–934.
- [20] S. Midha, S. Murab, S. Ghosh, Osteogenic signaling on silk-based matrices, Biomaterials 97 (2016) 133–136.
- [21] B. Marelli, C.E. Ghezzi, A. Alessandrino, J.E. Barralet, G. Freddi, S.N. Nazhat, Silk fibroin derived polypeptide-induced biomineralization of collagen, Biomaterials 33 (2012) 102–108.
- [22] C. Li, B. Hotz, S. Ling, J. Guo, D.S. Haas, B. Marelli, F. Omenetto, S.J. Lin, D.L. Kaplan, Regenerated silk materials for functionalized silk orthopedic devices by mimicking natural processing, Biomaterials 110 (2016) 24–33.
- [23] S. Das, F. Pati, Y.-J. Choi, G. Rijal, J.-H. Shim, S.W. Kim, A.R. Ray, D.-W. Cho, S. Ghosh, Bioprintable, cell-laden silk fibroin–gelatin hydrogel supporting multilineage differentiation of stem cells for fabrication of three-dimensional tissue constructs, Acta Biomater. 11 (2015) 233–246.
- [24] D. Su, M. Yao, J. Liu, Y. Zhong, X. Chen, Z. Shao, Enhancing mechanical properties of silk fibroin hydrogel through restricting the growth of β-Sheet domains, ACS Appl. Mater. Interfaces 9 (2017) 17489–17498.
- [25] N. Lin, L. Cao, Q. Huang, C. Wang, Y. Wang, J. Zhou, X.Y. Liu, Functionalization of silk fibroin materials at mesoscale, Adv. Funct. Mater. 26 (2016) 8885–8902.
- [26] B.M. Min, G. Lee, S.H. Kim, Y.S. Nam, T.S. Lee, W.H. Park, Electrospinning of silk fibroin nanofibers and its effect on the adhesion and spreading of normal human keratinocytes and fibroblasts in vitro, Biomaterials 25 (2004) 1289– 1297.
- [27] S. Das, F. Pati, Y.J. Choi, G. Rijal, J.H. Shim, S.W. Kim, A.R. Ray, D.W. Cho, S. Ghosh, Bioprintable, cell-laden silk fibroin–gelatin hydrogel supporting multilineage differentiation of stem cells for fabrication of three-dimensional tissue constructs, Acta Biomater. 11 (2015) 233.
- [28] A.E. Thurber, F.G. Omenetto, D.L. Kaplan, *In vivo* bioresponses to silk proteins, Biomaterials 71 (2015) 145–157.
- [29] F. Mottaghitalab, M. Farokhi, M.A. Shokrgozar, F. Atyabi, H. Hosseinkhani, Silk fibroin nanoparticle as a novel drug delivery system, J. Control. Rel. Off. J. Control. Rel. Soc. 206 (2015) 161.
- [30] J. Ge, K. Liu, W. Niu, M. Chen, M. Wang, Y. Xue, C. Gao, P.X. Ma, B. Lei, Gold and gold-silver alloy nanoparticles enhance the myogenic differentiation of myoblasts through p38 MAPK signaling pathway and promote in vivo skeletal muscle regeneration, Biomaterials 175 (2018) 19–29.

- [31] J. Yan, W. Zhou, Z. Jia, P. Xiong, Y. Li, P. Wang, Q. Li, Y. Cheng, Y. Zheng, Endowing polyetheretherketone with synergistic bactericidal effects and improved osteogenic ability, Acta Biomater. 79 (2018) 216–229.
- [32] H. Cao, W. Zhang, F. Meng, J. Guo, D. Wang, S. Qian, X. Jiang, X. Liu, P.K. Chu, Osteogenesis catalyzed by titanium-supported silver nanoparticles, ACS Appl. Mater. Interfaces 9 (2017) 5149–5157.
- [33] A.S. Lammel, X. Hu, S.-H. Park, D.L. Kaplan, T.R. Scheibel, Controlling silk fibroin particle features for drug delivery, Biomaterials 31 (2010) 4583–4591.
- [34] B. Cheng, Y. Yan, J. Qi, L. Deng, Z.-W. Shao, K.-Q. Zhang, B. Li, Z. Sun, X. Li, Cooperative assembly of a peptide gelator and silk fibroin afford an injectable hydrogel for tissue engineering, ACS Appl. Mater. Interfaces 10 (2018) 12474–12484
- [35] Y. Ding, M. Floren, W. Tan, Mussel-inspired polydopamine for bio-surface functionalization, Biosurf. Biotribol. 2 (2016) 121–136.
- [36] G. Xiang, J. Song, J. Ping, X. Zhang, X. Li, X. Xiao, M. Wang, S. Zhang, D. Yi, D. Feng, Polydopamine-templated hydroxyapatite reinforced polycaprolactone composite nanofibers with enhanced cytocompatibility and osteogenesis for bone tissue engineering, ACS Appl. Mater. Interfaces 8 (2016) 3499.
- [37] G. Jin, H. Qin, H. Cao, S. Qian, Y. Zhao, X. Peng, X. Zhang, X. Liu, P.K. Chu, Synergistic effects of dual Zn/Ag ion implantation in osteogenic activity and antibacterial ability of titanium, Biomaterials 35 (2014) 7699.
- [38] Q. Dong, H. Su, D. Zhang, In situ depositing silver nanoclusters on silk fibroin fibers supports by a novel biotemplate redox technique at room temperature, J. Phys. Chem. B 109 (2005) 17429–17434.
- [39] J. Zhou, B. Zhang, L. Shi, J. Zhong, J. Zhu, J. Yan, P. Wang, C. Cao, D. He, Regenerated silk fibroin films with controllable nanostructure size and secondary structure for drug delivery, ACS Appl. Mater. Interfaces 6 (2014) 21813– 21821
- [40] M.A. de Moraes, T. Crouzier, M. Rubner, M.M. Beppu, Factors controlling the deposition of silk fibroin nanofibrils during layer-by-layer assembly, Biomacromolecules 16 (2015) 97–104.
- [41] C. Shivanand, B.L. Rao, A. Pasha, Y. Sangappa, Synthesis of silver nanoparticles using Bombyx mori silk fibroin and their antibacterial activity, IOP Conf. Ser. Mater. Sci. Eng. (2016) 1–8.
- [42] S. Hofmann, C.T.W.P. Foo, F. Rossetti, M. Textor, G. Vunjak-Novakovic, D.L. Kaplan, H.P. Merkle, L. Meinel, Silk fibroin as an organic polymer for controlled drug delivery, J. Control. Rel. 111 (2006) 219–227.
- [43] C. Mona, F.C. Maria-Luisa, Q.G. Alba, A. Luis, S. Helmut, J.M. Navas, Comparative cytotoxicity study of silver nanoparticles (AgNPs) in a variety of rainbow trout cell lines (RTL-W1, RTH-149, RTG-2) and primary hepatocytes, Int. J. Environ. Res. Public Health 12 (2015) 5386–5392.
- [44] O. Rzhepishevska, S. Hakobyan, R. Ruhal, J. Gautrot, D. Barbero, M. Ramstedt, The surface charge of anti-bacterial coatings alters motility and biofilm architecture, Biomaterialsence 1 (2013) 589–602.
- [45] M. Ferreira, O. Rzhepishevska, L. Grenho, D. Malheiros, L. Gon? Alves, A.J. Almeida, L. Jord? O, I.A. Ribeiro, M. Ramstedt, P. Gomes, Levofloxacin-loaded bone cement delivery system: highly effective against intracellular bacteria and Staphylococcus aureus biofilms, Int. J. Pharm. 1 (2017) 241–248.
- [46] Z. Jia, P. Xiu, M. Li, X. Xu, Y. Shi, Y. Cheng, S. Wei, Y. Zheng, T. Xi, H. Cai, Bioinspired anchoring AgNPs onto micro-nanoporous TiO₂ orthopedic coatings: trap-killing of bacteria, surface-regulated osteoblast functions and host responses, Biomaterials 75 (2016) 203–219.
- [47] Z. Jia, P. Xiu, M. Li, X. Xu, Y. Shi, Y. Cheng, S. Wei, Y. Zheng, T. Xi, H. Cai, Bioinspired anchoring AgNPs onto micro-nanoporous TiO₂ orthopedic coatings: trap-killing of bacteria, surface-regulated osteoblast functions and host responses, Biomaterials 75 (2016) 203–222.
- [48] S.M. Baek, M.H. Shin, J. Moon, H.S. Jung, S.A. Lee, W.B. Hwang, J.T. Yeom, S.K. Hahn, H.S. Kim, Superior pre-osteoblast cell response of etched ultrafine-grained titanium with a controlled crystallographic orientation, Sci. Rep. 7 (2017) 44213–44316.
- [49] S. Mei, H. Wang, W. Wei, L. Tong, H. Pan, C. Ruan, Q. Ma, M. Liu, H. Yang, Z. Liang, Antibacterial effects and biocompatibility of titanium surfaces with graded silver incorporation in titania nanotubes, Biomaterials 35 (2014) 4255–4265.
- [50] Y. Li, Y. Liu, Y. Fu, T. Wei, G.L. Le, G. Gao, R.S. Liu, Y.Z. Chang, C. Chen, The triggering of apoptosis in macrophages by pristine graphene through the MAPK and TGF-beta signaling pathways, Biomaterials 33 (2012) 402–411.

- [51] C. Zheng, J. Wang, Y. Liu, Q. Yu, Y. Liu, N. Deng, J. Liu, Functional selenium nanoparticles enhanced stem cell osteoblastic differentiation through BMP signaling pathways. Adv. Funct. Mater. 24 (2015) 6872–6883.
- [52] G. Kaur, M.T. Valarmathi, J.D. Potts, Q. Wang, The promotion of osteoblastic differentiation of rat bone marrow stromal cells by a polyvalent plant mosaic virus, Biomaterials 29 (2008) 4074–4081.
- [53] T. Lu, X. Liu, S. Qian, H. Cao, Y. Qiao, Y. Mei, P.K. Chu, C. Ding, Multilevel surface engineering of nanostructured TiO₂ on carbon-fiber-reinforced polyetheretherketone, Biomaterials 35 (2014) 5731–5740.
- [54] M. Tirrell, E. Kokkoli, M. Biesalski, The role of surface science in bioengineered materials, Surf. Sci. 500 (2002) 61–83.
- [55] R. Zhang, P. Lee, V.C. Lui, Y. Chen, X. Liu, C.N. Lok, M. To, K.W. Yeung, K.K. Wong, Silver nanoparticles promote osteogenesis of mesenchymal stem cells and improve bone fracture healing in osteogenesis mechanism mouse model, Nanomed.: Nanotechnol., Biol. Med. 11 (2015) 1949–1959.
- [56] Y. Wang, R. Aun, F.L. Tse, Absorption of p-glucose in the rat studied using in situ intestinal perfusion: a permeability-index approach, Pharm. Res. 14 (11) (1997) 1563–1567.
- [57] S. Ghanaati, C. Orth, R.E. Unger, M. Barbeck, M.J. Webber, A. Motta, C. Migliaresi, K.C. James, Fine-tuning scaffolds for tissue regeneration: effects of formic acid processing on tissue reaction to silk fibroin, J. Tissue Eng. Regenerat. Med. 4 (2010) 464–472.
- [58] M.A. Lopez-Heredia, E. Goyenvalle, E. Aguado, Bone growth in rapid prototyped porous titanium implants, J. Biomed. Mater. Res. Part A 85A (2008) 664–673.
- [59] S. Ponader, W.C. Von, M. Widenmayer, R. Lutz, P. Heinl, C. Körner, R.F. Singer, E. Nkenke, F.W. Neukam, K.A. Schlegel, *In vivo* performance of selective electron beam-melted Ti-6Al-4V structures, J. Biomed. Mater. Res. Part A 92A (2010) 56–62.
- [60] T. Kokubo, H. Takadama, How useful is SBF in predicting in vivo bone bioactivity? Biomaterials 27 (2006) 2907–2915.
- [61] V.M. Frauchiger, F. Schlottig, B. Gasser, M. Textor, Anodic plasma-chemical treatment of CP titanium surfaces for biomedical applications, Biomaterials 25 (2004) 593–606.
- [62] A. LealEgaña, T. Scheibel, Silk-based materials for biomedical applications, Biotechnol. Appl. Biochem. 55 (2010) 155–167.
- [63] H. Hu, Z. Li, M. Lu, X. Yun, W. Li, C. Liu, A. Guo, Osteoactivin inhibits dexamethasone-induced osteoporosis through up-regulating integrin $\beta 1$ and activate ERK pathway, Biomed. Pharmacotherapy 105 (2018) 66–72.
- [64] Y.K. Seo, H.H. Yoon, Y.S. Park, K.Y. Song, W.S. Lee, J.K. Park, Correlation between scaffold in vivo biocompatibility and in vitro cell compatibility using mesenchymal and mononuclear cell cultures, Cell Biol. Toxicol. 25 (2009) 513–522.
- [65] O. Hakimi, T. Gheysens, F. Vollrath, M.F. Grahn, D.P. Knight, P. Vadgama, Modulation of cell growth on exposure to silkworm and spider silk fibers, J. Biomed. Mater. Res. Part A 92A (2010) 1366–1372.
- [66] H. Qin, C. Zhu, Z. An, Y. Jiang, Y. Zhao, J. Wang, X. Liu, B. Hui, X. Zhang, Y. Wang, Silver nanoparticles promote osteogenic differentiation of human urine-derived stem cells at noncytotoxic concentrations, Int. J. Nanomed. 9 (2014) 2469.
- [67] A.C. Macintosh, V.R. Kearns, A. Crawford, P.V. Hatton, Skeletal tissue engineering using silk biomaterials, J. Tissue Eng. Regen. Med. 2 (2008) 71.
- [68] B.B. Mandal, S.C. Kundu, Osteogenic and adipogenic differentiation of rat bone marrow cells on non-mulberry and mulberry silk gland fibroin 3D scaffolds, Biomaterials 30 (2009) 5019–5030.
- [69] M. Mizuno, R. Fujisawa, Y. Kuboki, Type I collagen-induced osteoblastic differentiation of bone-marrow cells mediated by collagen-alpha2beta1 integrin interaction, J. Cell. Physiol. 184 (2000) 207.
- [70] S. Ghanaati, C. Orth, R.E. Unger, M. Barbeck, M.J. Webber, A. Motta, C. Migliaresi, C. James Kirkpatrick, Fine-tuning scaffolds for tissue regeneration: effects of formic acid processing on tissue reaction to silk fibroin, J. Tissue Eng. Regen. Med. 4 (2010) 464–472.
- [71] S.-R. Jung, N.-J. Song, D.K. Yang, Y.-J. Cho, B.-J. Kim, J.-W. Hong, U.J. Yun, D.-G. Jo, Y.M. Lee, S.Y. Choi, Silk proteins stimulate osteoblast differentiation by suppressing the Notch signaling pathway in mesenchymal stem cells, Nutrit. Res. 33 (2013) 162–170.
- [72] J. Chang, W. Sonoyama, Z. Wang, Q. Jin, C. Zhang, P.H. Krebsbach, W. Giannobile, S. Shi, C.-Y. Wang, Noncanonical Wnt-4 signaling enhances bone regeneration of mesenchymal stem cells in craniofacial defects through activation of p38 MAPK, J. Biol. Chem. 282 (2007) 30938–30948.